Energy Conversion and Management: X 28 (2025) 101367

Contents lists available at ScienceDirect

Energy Conversion and Management: X

journal homepage: www.sciencedirect.com/journal/energy-conversion-and-management-x

Techno-economic analysis of a novel hybrid wind-wave floating platform concept: The OctaPlat

M.B.V.A. Rodrigues [a], J.C.C. Portillo [b,*], J.C.C. Henriques [c], L.M.C. Gato [c], N.P. Mendonça [a]

[a] Instituto Superior Técnico, Universidade de Lisboa, Av. Rovisco Pais 1, 1049-001 Lisbon, Portugal
[b] Laboratório Nacional de Energia e Geologia, I.P. Estrada da Portela, Bairro do Zambujal Ap 7586, 2610-999, Amadora, Portugal
[c] IDMEC, Instituto Superior Técnico, Universidade de Lisboa, Av. Rovisco Pais 1, 1049-001 Lisbon, Portugal

ARTICLE INFO

Keywords:
Hybrid wind-wave energy systems
Offshore wind energy
Floating multi-purpose platforms
Oscillating water column
Modelica
OctaPlat

ABSTRACT

This work focuses on the techno-economic analysis of a novel floating offshore hybrid wind-wave platform. Floating multi-purpose platforms can potentially reduce costs associated with floating offshore wind. This work is based on the OctaPlat, a barge-type hybrid wind-wave floating platform designed at Instituto Superior Técnico, University of Lisbon. The paper presents the concept and numerical model of the floating wave platform, comprising five oscillating water column (OWC) wave energy converters, which was implemented in the object-oriented non-causal Modelica language. The OctaPlat configuration investigated here was equipped with the 15 MW IEA reference wind turbine, whose power output was computed using OpenFAST©. A sensitivity analysis of the geometry was performed, and the best performer design reached an average annual wave turbine power of 2.5 MW and a total wind-wave power of about 10.75 MW for a selected site off the west coast of Portugal. The levelized cost of energy (LCOE) was determined for a farm in the selected location. Various scenarios were assessed, and a Monte Carlo approach resulted in a probable value of LCOE of 135 €/MWh, with $\mathrm{LCOE_{P90}}$ and $\mathrm{LCOE_{P10}}$ values of 99 and 180 €/MWh, respectively. Experimental tests of the wave energy conversion systems were performed on a scale of 1:100, and comparisons with numerical results showed good agreement, with a coefficient of determination (R^2) of approximately 0.94 and relative differences were less than 20%, except for a few peak deviations. These results reveal the potential competitiveness of wind-wave multi-purpose platforms in floating offshore renewable energy projects.

1. Introduction

The global surface temperature increased around 1.1 °C from 1850–1900 to 2011–2020 [1]. Greenhouse gas emissions are considered the main drivers of this human-induced phenomenon, with the largest share belonging to CO_2 emissions from fossil fuels combustion and industrial processes [1]. Established in 2015, the Paris Agreement called for actions to limit global warming to 1.5 °C, implying emissions to reach net zero by 2050. Policymakers worldwide are, therefore, seeking to increase the adoption rate of energy technologies from low-carbon sources [2].

In this sense, the European Commission (EC) set a package of policy initiatives to make Europe the first climate-neutral continent [3]. Encouraged by policy support and market developments, renewables have seen significant growth in recent years [4]. Upon the commencement of Russia's war in Ukraine and the inherent challenge of maintaining energy security, it became clear that this development needed further accelerated. In 2022, the European Commission responded by releasing the REPowerEU strategy, which proposed increasing the European Union's 2030 target for renewables from 40% to 45% [4].

Offshore energy arises as an answer to these challenges. European Research and Development (R&D) organizations and industries are currently working to develop technologies to harness the power of the sea and produce clean electricity at competitive prices. The European Union (EU) has the most extensive maritime area in the world. It is in an advantageous position to develop offshore renewable energy due to its seas' diversity and complementary nature. Pursuing this path is crucial if Europe is to meet its proposed targets by 2050 [5].

Offshore wind technology has emerged as a key player in the path to decarbonization, and its development has enabled countries to build farms in locations with high wind resources close to densely populated

* Corresponding author at: Laboratório Nacional de Energia e Geologia, I.P. Estrada da Portela, Bairro do Zambujal Ap 7586, 2610-999, Amadora, Portugal.
E-mail addresses: mariana.beirao.rodrigues@tecnico.ulisboa.pt (M.B.V.A. Rodrigues), juan.portillo@lneg.pt (J.C.C. Portillo), joaochenriques@tecnico.ulisboa.pt (J.C.C. Henriques), luis.gato@tecnico.ulisboa.pt (L.M.C. Gato), nuno.mendonca@tecnico.ulisboa.pt (N.P. Mendonça).

https://doi.org/10.1016/j.ecmx.2025.101367
Received 22 August 2025; Received in revised form 18 October 2025; Accepted 27 October 2025
Available online 31 October 2025

Nomenclature

Romans

a	Generator control law constant [W(s/rad)^3]
A^∞	Added mass at infinite frequency [kg]
$A_\mathrm{w}(\omega_n)$	Wave amplitude as function of the wave frequency ω_n [m]
c_v	Specific heat at constant volume J/(kg K)
d_t	Turbine rotor diameter [m]
f_o	Probability of occurrence [%]
F_m^exc	Excitation force on body m [N]
F_m^moor	Force of the moorings on body m [N]
F_m^PTO	Force of the m PTO system [N]
g	Acceleration of gravity [m/s^2]
H_s	Significant wave height [m]
I	Turbine generator set moment of inertia [kg m^2]
m_i	Mass of body i [kg]
$\dot{m}_\mathrm{t}$	Turbine mass flow rate [kg/s]
p	Pressure [Pa]
p_ac	Relative air chamber pressure [Pa]
p_at	Absolute atmospheric pressure [Pa]
$\bar{P}^\mathrm{ann}$	Mean annual pneumatic power [W]
P_ctrl	Generator shaft power [W]
P_p	Pneumatic power [W]
P_t	Turbine shaft power [W]
R_{ij}	Radiation damping force on body i due to body j [N]
$S_{\mathrm{p},m}$	OWC water plane area of piston m [m^2]
t	Time [s]
V_0	Volume of air inside the chamber in calm water [m^3]
V_c	Instantaneous air chamber volume [m^3]
U_wind	Wind speed [m/s]
x_i	Position of DoF i [m, rad]
$\dot{x}_i$	Velocity of DoF i [m/s, rad/s]
$\ddot{x}_i$	Acceleration of DoF i [m/s^2, rad/s^2]

Greek symbols

Γ_i	Excitation force on body i per unit wave height [N/m]
Π	Turbine dimensionless power [–]
ρ	Density [kg/m^3]
ρ_at	Air density in atmospheric conditions [kg/m^3]
$\rho_\mathrm{a,in}$	Stagnation air density at turbine inlet conditions [kg/m^3]
ρ_w	Water density [kg/m^3]
Φ	Turbine dimensionless flow rate [–]
ϕ_r	Random phase of the wave [rad]
Ψ	Turbine dimensionless pressure head [–]
ω	Wave frequency [rad/s]
Ω	Rotational speed [rad/s]

Subscripts

at	Atmospheric quantity
bep	Best efficiency point
ac	Air chamber
in	Turbine inlet conditions
p	Pneumatic value
t	Turbine quantity

Acronyms

DoF	Degree-of-Freedom
FOWT	Floating Offshore Wind Turbine
LCOE	Levelized Cost of Energy
PTO	Power Take-Off
SWL	Still Water Level

coastal areas [6]. The higher capacity factor of offshore wind and its seasonal patterns confer greater security to the system compared to other variable renewable energy sources [7]. All of these benefits contribute to an increasing adoption of this technology, encouraged by governments' policies and incentives. To comply with the Net Zero Emissions (NZE) scenario by 2050, and assuming the sector makes significant progress in the coming years, the International Renewable Energy Agency (IRENA) states that offshore wind capacity could reach 228 GW by 2030 and 1000 GW by 2050, with Asia accounting for more than 60% of global installations [6]. Therefore, facing the challenges imposed by the energy crisis, the Portuguese government announced its target of 2 GW of offshore wind energy capacity by 2030 [8].

However, offshore wind must undergo significant technological development to verify this growth. In fact, since the first offshore wind deployment, efforts have been made to develop more efficient turbines [7]. Such innovation has contributed to increasing the maximum power output of turbines by increasing the hub height and swept area, which enables the turbine to have a higher wind capture rate and, ultimately, to lower the Levelized Cost of Energy (LCOE). In addition, offshore wind installations have moved further from shore to access better quality wind resources, translating into higher capacity factors [7,9]. However, this implies that projects are installed in deeper waters, which presents new deployment challenges and makes them economically unattractive compared to the fixed-bottom foundations used in shallow water projects. The industry has therefore developed floating foundation technologies, based on previous examples from the Oil and Gas sector, and assessed their costs [7]. Despite the recent advances regarding this technology, the LCOE of floating offshore wind is still considerably higher than that of bottom-fixed solutions [7,10,11]. In fact, according to IRENA's 2024 report on the matter [12], floating offshore wind's LCOE is currently around 170 EUR/MWh, nearly 4 times that of bottom-fixed turbines. The EU Blue Economy Report of 2025 further emphasizes the strong project-specific variability of the LCOE. For instance, in 2020–2023, the LCOE was 145 EUR/MWh for Hywind Tampen in Norway and 240 EUR/MWh for Wind Float Atlantic in Portugal [13]. Thus, to unlock access to higher-quality wind resources in deep waters, further cost reductions are essential. One possibility is to develop systemic approaches with ocean energy technologies [6], which benefit from greater predictability than other Offshore Renewable Energy (ORE) sources [7].

Combined wind-wave systems can be classified according to the technology, water depth, or location relative to the shoreline. Ref. [14] proposes a classification based on the level of connectivity, see Fig. 1. Accordingly, these systems are categorized as co-located, hybrid, and island systems.

This study focuses on floating hybrid wind-wave systems. These benefit from being exposed to the higher wave resources that occur in deeper waters and the potential to harvest better quality winds. Furthermore, these hybrid systems have the potential to become cost-effective solutions for offshore power supply [16]. By sharing the

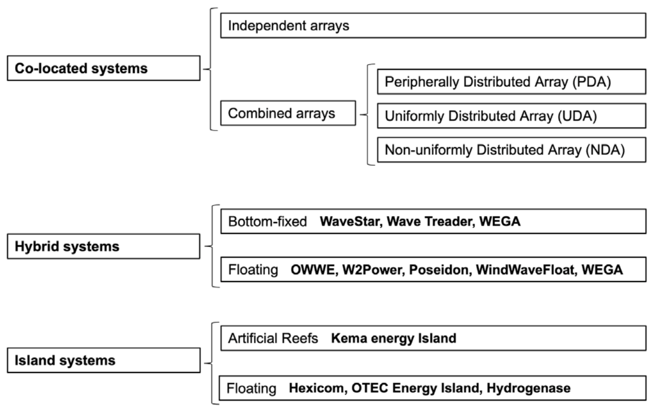

Fig. 1. Different types of combined wind-wave systems [14,15].

same platform, hybrid systems have the potential to reduce capital expenditure (CAPEX) and operational expenditure (OPEX) by leveraging synergies. Moreover, floating wind systems face several challenges for full-scale deployment, such as increased fluctuations in offshore wind speed, the motion of the platform, and the turbine's response to changing wind conditions. Effective power smoothing is therefore critical to ensure stable and reliable grid integration [17]. Hybrid configurations can help address these challenges since wave climate peaks typically trail the wind peaks, resulting in a smoother combined power output that reduces variability and improves forecast accuracy [18]. To further manage power fluctuations, hybrid systems can incorporate short-term storage solutions such as battery energy storage systems (BESS) or convert surplus power into hydrogen via electrolysis [17]. The latter provides a pathway for long-term energy storage and other applications such as sustainable fuels production offshore [19].

Several floating hybrid wind-wave energy systems have been conceptualized, and tested during recent years. Dong et al. [20] presents a review of hybrid wind-wave energy systems, with about 40 different concepts, most of them representing just ideas without great development, with about half tested at a small scale in laboratory environments. Poseidon Wave and Wind by Floating Power Plant, and W2Power by Pelagic Power have reached demonstration scale ocean deployments [14]. The Poseidon system is a buoyancy-stabilized platform that integrates three wind turbines with multiple WECs. The platform's length can vary between 80 to 150 m, depending on site-specific requirements. A 37-m scale model was tested offshore Denmark, equipped with ten 3 kW WECs and three 11 kW wind turbines. The full-scale Poseidon system is designed to generate approximately 2.6 MW from oscillating water columns and an additional 2.3–5 MW from wind turbines [14]. W2Power is a floating hybrid system that combines two wind turbines mounted on a semi-submersible platform with multiple heave-type point absorber WECs. This configuration aims to maximize energy capture from both wind and wave resources while ensuring platform stability [14]. Other studies focused on bottom-fixed hybrid wind-wave systems [21–23]. For example, Pérez-Collazo et al. [21] considered and designed three prototypes: OWC-monopile, OWC-jacket frame, and oscillating body-monopile.

Hybrid wind–wave systems have been investigated in several studies, many of which highlighting potential improvements in energy yield and hydrodynamic performance [16,24–28]. For instance, a hybrid system combining two types of WECs with DeepCwind [29] achieved a total power production at least 27.2% higher than that for the Floating Offshore Wind Turbine (FOWT) alone [24]. In addition to reduced motions and increased stability, the wind turbine power generation capacity was optimized at both rated and below-rated operating conditions. Other studies [25,26] reported lower pitch movements for FOWTs with integrated WECs. Recently, Zhang et al. [30] experimentally compared the dynamic responses of a conventional FOWT and a floating wind-wave-tidal (WWT) system under regular, irregular, and freak waves. Results showed that, under long-period regular waves, the WWT system achieved substantial pitch motion reductions relative to the FOWT, with amplitudes decreased by 70.2% at the heave natural period and 94.6% at the pitch natural period. Although motion responses of both systems increased with wave height, the WWT system maintained superior performance, achieving up to 37.12% lower pitch amplitudes across different spectral peak periods and a maximum reduction of 44.7% under long-period freak waves. These improvements were primarily attributed to the damping contribution of the integrated WECs, which dissipate wave energy through frequent water entry and exit interactions. While the addition of WECs led to higher heave responses and mooring tensions, the WWT system exhibited significantly enhanced hydrodynamic robustness overall.

Another study [27] evaluated a hybrid wind-wave platform integrating a semi-submersible Nautilus platform [31] with four-point absorbers, concluding that pitch motion and nacelle acceleration were reduced, enhancing stability. While wind turbine power output remained nearly unchanged, the hybrid system produced additional energy from wave conversion. In addition to demonstrating the reduced pitch motion of the studied floating platform, Hu et al. [16] aimed to optimize the size and layout of the WECs within the hybrid system. The authors concluded that larger WECs are preferable as they allow more wave energy to be captured in a limited area and sea state.

While some studies indicate improved stability with hybrid designs, others highlight challenges. Faraggiana et al. [32] worked on achieving the optimal design of a semisubmersible hybrid wind-wave floating platform integrating three WECs with the goal of increasing energy production while improving structural stability and reducing costs when compared to the standalone FOWT. The system consists of a central cylinder with three WECs connected via arms, offering dynamic stability to the platform. The authors studied different geometries for the WECs — cylindrical, semi-cylindrical and spherical — and made a sensitivity analysis on their main design parameters. The cylindrical WEC shape with a large radius and small height was found optimal. The power increase of the hybrid design is about 14.3% (7.5% from WECs and 6.8% from wind turbine) when compared to the standalone system. However, it was found that for less energetic sea states, the floating wind turbine alone showed a better dynamic stability compared to the hybrid system. In fact, some studies found an increase in the platform's motion when integrating WECs as opposed to other findings. Muliwan et al. [33], for instance, who studied a hybrid spar platform with an integrated two-body axi-symmetric floating WEC, found that the hybrid system had greater mooring and tower loading in survival conditions resulting from WEC loading in rough seas. This raises challenges, as it shows that if not carefully designed and integrated in the platform, the WECs can harm its stability, rather than help suppress its motion, as pointed in other studies.

Beyond hydrodynamic performance, the techno-economic feasibility of hybrid wind–wave systems is a key factor determining their potential deployment at commercial scale. While early studies primarily focused on single-source systems such as floating wind or wave energy converters, the combined assessment of hybrid platforms remains comparatively limited. Nevertheless, available evidence indicates that the LCOE of hybrid systems can be lower than that of their standalone counterparts. This reduction arises from several interacting factors, including the sharing of assets both onshore and offshore, the complementarity between wind and wave resources that increases the annual energy yield, and the sharing of operational and maintenance logistics, which further lowers operational costs [34]. As a result, hybrid wind–wave configurations have demonstrated economic advantages. For example, the semi-submersible Nautilus-based platform integrating four point absorbers yielded a 9% lower LCOE compared with the floating wind turbine alone, with the potential for a 12% reduction in larger-scale deployments [27]. Industry analyses also support these findings, indicating that that shared infrastructure and services between offshore wind and wave energy developments could reduce overall LCOE of offshore wind by up to 12% [18].

Finally, material selection for substructures also plays a role in the feasibility of hybrid platforms. Most substructures for offshore wind currently considered are made of steel, as it is the case for Principle Power's Wind Float [35] used in projects such as the Wind Float Atlantic, the first offshore wind project using a semisubmersible platform [36]. A report published by DNV [37] performed a comparative analysis between steel and concrete substructures for floating offshore wind. The study considers carbon footprint, cost, and potential for local content and studied spar and semisubmersible platforms. The results showed that concrete floaters, both spar and semi-submersible, have lower carbon footprint and costs, than their steel counterparts. Notably, recent projects are now adopting concrete platforms — one of the two sites awarded as part of the Mediterranean tender (AO6) in France at the end of 2024 [38], uses the BW Ideol barge-type platform made of concrete. While previous studies highlight the benefits of floating hybrid wind-wave systems, challenges such as structural loading, stability, and cost-effectiveness remain.

This paper introduces OctaPlat, a novel hybrid wind-wave system that aims to harness all the benefits of hybrid systems while addressing their potential limitations and offering a viable solution for offshore renewable energy generation. Fig. 2 presents a schematic representation of an OctaPlat. The work focuses on the techno-economic analysis of the system to assess its potential feasibility. Section 3 contains the methods followed in the study and the tools and materials used. It further presents the wind turbine properties used for this study and the farm's location and layout. Afterwards, the numerical modeling equations are given in Section 4. Section 5 outlines the base case's definition and analysis, considering the platform's design, properties, and results obtained for that scenario. It further includes a brief comparison between experimental and numerical results. A sensitivity analysis is presented in Section 6, followed by the determination of the LCOE of the wind farm for the best-chosen scenario in Section 7. The conclusions are presented in Section 8.

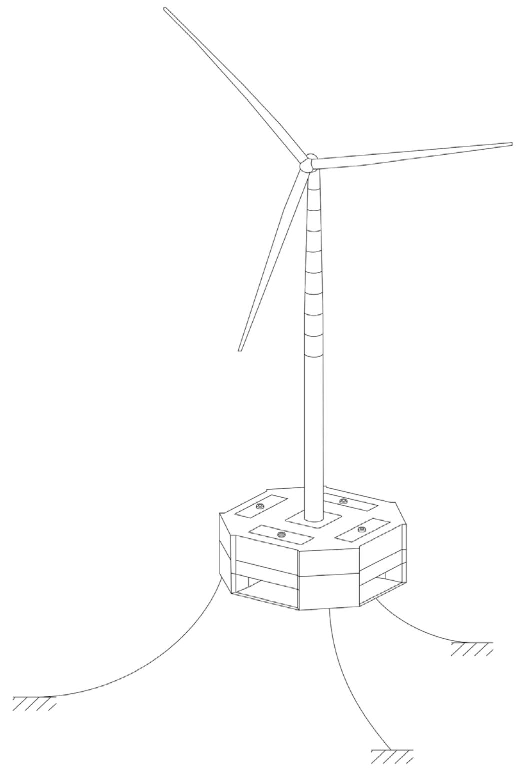

Fig. 2. Conceptual representation of the hybrid wind-wave system — OctaPlat. The floating platform converts wave energy through five oscillating water columns, and a wind turbine is mounted on the platform, which is moored using four mooring lines.

Table 1
General properties of the platform.

Parameter	Units	Value
Displaced volume	m^3	71,534
Structure mass (Concrete)	kg	50.7×10^6
Transition tube mass (Steel)	kg	898×10^3
Seawater ballast mass	kg	19.3×10^6
Draft	m	20.3
Vertical CG from SWL	m	−8.56
Vertical CB from SWL	m	−8.88
Roll inertia (CG)	$kg\,m^2$	7.31×10^{10}
Pitch inertia (CG)	$kg\,m^2$	4.61×10^{10}
Yaw inertia (CG)	$kg\,m^2$	4.73×10^{10}

2. The OctaPlat

The definition of the geometry and design of the barge-type floating platform — OctaPlat — conceived at Instituto Superior Técnico is presented here. The conceptual design (see Fig. 2) considers the installation of the IEA-15-240-RWT 15 MW reference wind turbine. The system, with an octahedral shape made of concrete, has an 84 m long and five OWCs. Four lateral rectangular shaped OWCs around the periphery of the platform, with main dimensions of 35 m long and 11 m wide, and a central OWC of 304 m^2. For the lateral OWCs, the water enters through a cavity of 39 m long and 11 m high, which narrows until it reaches the 35 m long base. The turbines selected for the OWC are impulse air turbines. Once in place, the platform has a draft of about 20 m with a 15 m upper section above the still water level (SWL). The platform's model created in a CAD system is presented in Fig. 3, and its general properties are in Table 1. A cut view of the platform with seawater ballast is also presented. The platform is designed to support the wind turbine between the central OWC and one of the lateral ones. Thus, to keep it in the upright position, four sections are created to allow ballast separation: the submerged part of the platform includes four diagonal walls running from each corner of the central OWC to the end of the structure, as seen in Fig. 3.

The total mass of the platform is 70,902 t, of which 50,717 t corresponds to the concrete structure, 898 t to a transition piece (a 16 cm thick tube [39] to support the turbine tower along the 15 m of the upper part of the platform) made of steel, and 19,287 t of seawater ballast distributed in such a way that maintains the platform in the upright position. It should be noted that neither the platform nor the transition piece is designed in detail, and a structural analysis should be performed in the future. Despite the high mass of concrete obtained, it is important to note that typical offshore structures from the Oil & Gas industry can reach similar masses [40].

The total mass of the platform reaches 73,322 t when the wind turbine and ballast are included. The mass of the wind turbine accounts for 2419 t. The overall center of gravity (CoG) is at −1.4 m, and the metacentric height obtained is about 24 m.

3. Methodology

An overview of the methodology used in this work is presented in Fig. 4. It allows the relative comparison of different platform geometries regarding the OWC systems, and once selected a best-performer within the constraints of the sensitivity analysis, the techno-economic analysis follows. The latter is done using the Levelized Cost of Energy (LCOE) as the main indicator. A Monte Carlo probabilistic analysis was performed for the best case, considering variations of CAPEX, OPEX, AEP, and discount rate. In addition, an exploratory assessment was conducted to evaluate different air turbine damping (i.e., different sizes) for each OWC, rather than using the same damping for all OWCs.

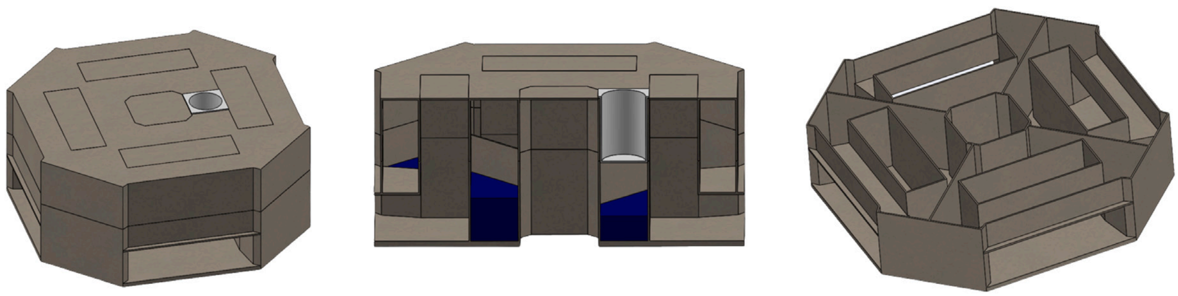

Fig. 3. CAD model of the platform. Left: perspective view; middle: lateral cross section; right: plane cross section at water level.

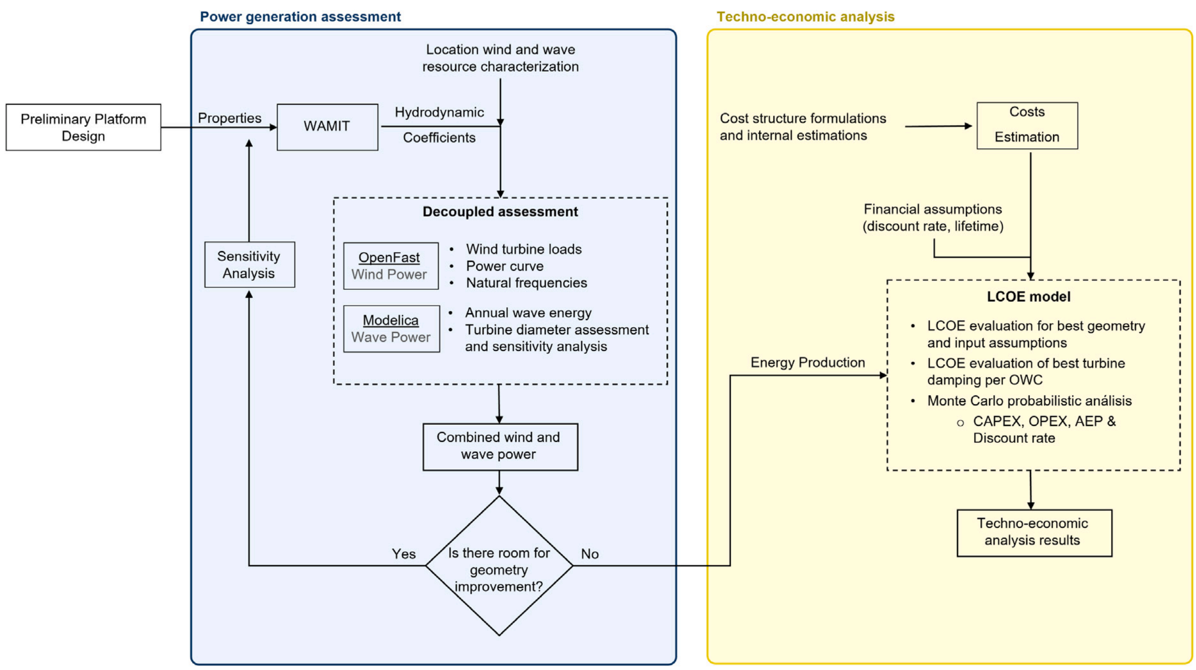

Fig. 4. Methodology for the design and analyses of the hybrid wind-wave energy system.

An initial design of the hybrid platform was made based on the preliminary system developed at the Instituto Superior Técnico. The platform was modeled in a CAD system which allowed to retrieve its properties, i.e., mass, displaced volume, centers of gravity and buoyancy, and inertias. The design was then input into WAMIT©, which is a 3D Panel Method code (based on the boundary integral equation method (BIEM)) used to compute wave radiation and wave excitation on the offshore structure in the frequency domain [41]. It is based on the linear and second-order potential flow theory for analyzing floating or submerged bodies in the presence of ocean waves, considering the system to be rigid [41]. From WAMIT©, it was thus possible to obtain the hydrodynamic coefficients of the floating platform and the oscillating water columns (OWCs) wave energy converters. These results, together with the wind and wave resource characterization of the deployment site, were utilized in OpenFAST©, for the wind energy extraction assessment and in an OpenModelica tool developed at Instituto Superior Técnico (IST) [42] for the wave energy production analysis.

OpenFAST© is an open-source aero-hydro-servo-elastic time-domain simulation tool developed by NREL [43]. This tool is utilized to assess the loads on the turbine, determine the average power produced for different wind speeds (and, therefore, obtain the turbine's power curve), and perform free decay tests to determine the natural periods for each degree of freedom (DoF) of the platform. The feasibility of the project heavily relies on the wind turbine, which generates the majority of the power in the hybrid system. It was, therefore, crucial to understand the OWCs' impact on its behavior. Although OpenFAST© is not able to model the OWCs and their respective coupling forces to the floater, it allows the loads on the turbine and the power generation to be to determined using the hydrodynamic coefficients of the hybrid platform. On the other hand, the IST's OpenModelica-based tool [42] allows the analysis of the wave energy production of the system.

As a result of the simulation, it was possible to verify the annual energy produced and the influence that different OWCs' turbine damping coefficients have on this value. These two outcomes were then coupled to determine the total power production of the system. In case there was room for improvement, the geometry of the platform was re-assessed, and the new hydrodynamic coefficients were computed using WAMIT©. Otherwise, its geometry and design were finished, and a techno-economic analysis followed.

It is worth mentioning that, due to the high computational complexity associated with fully coupled simulations, the power generation analysis model in this study does not account for the coupling forces between the OWCs and the wind turbine on the platform motion response. Although the present model enables an efficient preliminary evaluation of the hybrid platform's overall power performance, it may introduce deviations in predicted motion responses and power outputs, as mutual interactions between hydrodynamic and aerodynamic loads can alter the floater's behavior and no real-time coupling is implemented.

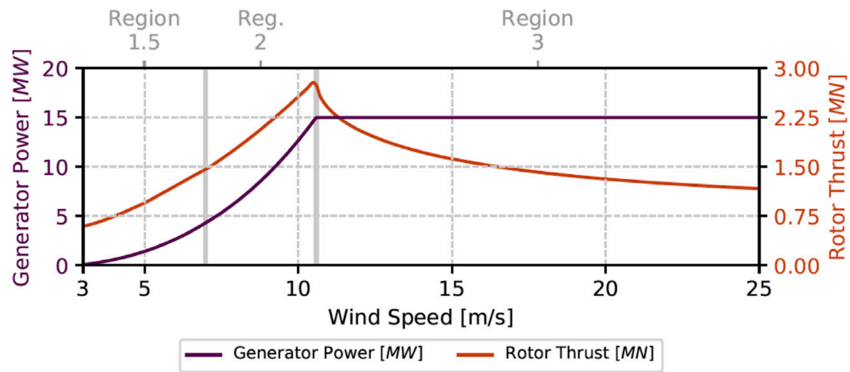

Fig. 5. Power curve of the IEA 15 MW reference turbine.
Source: Reproduced from [44].

Fig. 6. Wind farm location.

3.1. IEA 15 MW offshore reference turbine

The 15 MW reference offshore wind turbine developed by the IEA and jointly designed by NREL, the Technical University of Denmark (DTU), and the University of Maine [44] was selected. This is a conventional 3-bladed variable speed, pitch-regulated Horizontal Axis Wind Turbine with 15 MW of rated power, a rotor diameter of 240 m and a hub height of 150 m. The rated wind speed is 10.6 m/s with a design tip-speed ratio of 9.0 m/s. Cut-in and cut-out speeds are 3 m/s and 25 m/s, respectively (see Fig. 5). A complete description of the turbine can be found in Ref. [44].

3.2. Location details and hybrid wind-wave farm layout

The designated site is located 35 km off the west coast of mainland Portugal, near Porto and the Port of Leixões, at the coordinates of 41° 10′27"N 9° 03′50"W (Fig. 6). This site is close to an area that has been earmarked for future offshore wind projects [45].

Table 2 provides a comprehensive breakdown of the joint wind speed and sea states with probabilities of occurrence.

The data in Table 2 is derived from the statistical treatment of the joint wind and wave data at the location from January 1979 to December 2009 obtained from the National Oceanic and Atmospheric Administration (NOAA) Wavewatch III© hindcast data [46–48]. The procedure involved the creation of (i) wind classes and their probabilities of occurrence, (ii) the association of mean values of significant wave heights per wind class, and (iii) the association of mean peak period per each wind class. This is deemed a minimum viable procedure for estimating the FOWT behavior in the selected site. It should be noted that more detailed studies should consider extended methods that more accurately account for sea state variability per wind class. It is done in more advanced stages of offshore wind turbines' design and certification processes.

Table 2
Wind and wave conditions at the selected site and wind class probability of occurrence f_{o1}.

U_{wind} [m/s]	H_s [m]	T_p [s]	f_{o1} [%]	U_{wind} [m/s]	H_s [m]	T_p [s]	f_{o1} [%]
1	1.7	11.4	1.76	14	2.9	10.9	4.04
2	1.7	11.3	3.19	15	3.1	10.9	3.17
3	1.7	11.3	4.88	16	3.3	11.0	2.39
4	1.7	11.3	6.60	17	3.6	11.1	1.75
5	1.8	11.3	7.93	18	3.8	11.2	1.25
6	1.8	11.2	8.87	19	4.0	11.4	0.83
7	1.9	11.3	9.25	20	4.4	11.5	0.54
8	2.0	11.2	8.89	21	4.7	11.7	0.37
9	2.1	11.2	8.14	22	4.9	11.8	0.22
10	2.2	11.2	7.57	23	5.3	12.0	0.14
11	2.3	11.0	6.88	24	5.4	12.0	0.10
12	2.5	10.9	6.11	25	5.6	11.9	0.04
13	2.6	10.9	5.01				

Table 3
Reduced wave climate at the selected site and sea states probability of occurrence f_{o2}, see [49,50].

H_s [m]	T_p [s]	f_{o2} [%]	H_s [m]	T_p [s]	f_{o2} [%]
1.1	6.4	7.04	2.1	13.5	0.59
1.2	7.6	12.35	3.1	9.4	9.41
1.2	9.0	8.17	3.2	11.6	10.07
1.9	7.4	11.57	3.3	13.8	2.57
2.0	9.3	20.66	4.8	11.5	4.72
2.1	11.4	8.61	4.9	14.0	2.81

Table 2 is considered for wind conversion simulations. For wave energy conversion, Table 3 is utilized [49,50]. This table consists of 12 sea states, which represent the selected site. The procedure followed to obtain this equivalent reduced number of sea states is presented in Ref. [51].

The wind-wave farm layout considered in this work is based on the Lillgrund wind farm, reported in Ref. [52], later used in Ref. [53], which utilized the same site for its analyses. The northwest orientation was chosen for the hybrid farm because of the prevailing northwesterly wind direction at the selected site. The farm layout is described by a spacing of consecutive turbines in a row of 4.3D, where D is the wind turbine rotor diameter. The spacing between each row is 3.3D, as reported for the Lillgrund wind farm in the Öresund region [52].

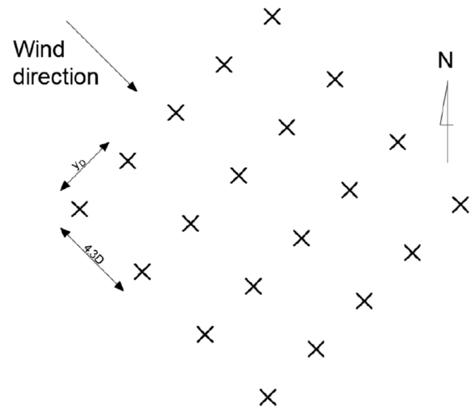

Fig. 7. Layout of the wind farm, where D is the turbine rotor diameter and y_D is the distance between rows [53].

Despite the potential to significantly increase the wake losses of a wind farm, the clustering of wind turbines is associated with lower costs (array cables, sea lease, and site clearance) [52,53]. Furthermore, the excessively tight layout might increase fatigue loads, translating into a lower lifetime of the farm. The study of these loads is beyond the scope of the present work.

Fig. 7 presents the layout considered for the farm used for the techno-economic analysis performed later. The layout comprises twenty turbines (as described in Section 3.1). The turbines are distributed in five rows of 4 turbines each.

4. Numerical modeling - Rigid array of five OWCs integrated in a floating platform

This section presents the approach adopted for the wave energy systems' modeling, implemented in the object-oriented equation-based Modelica language, similar to the model presented in Ref. [42]. As explained above, the floating wind turbine modeling was performed in OpenFAST©, and the mathematical description of the model is presented in Ref. [43].

The hydrodynamic coefficients that are used as input were calculated using WAMIT© and were entered into OpenFAST© and the OpenModelica wave platform model. The main results are presented in Sections 5.1 and 5.2. The OpenModelica wave platform model presented in Section 4 was partially validated through experimental test results (see Appendix B).

4.1. Equations of motion

The motion of a generic floating body subject to incident waves is studied under the assumption that the waves are described by the linear wave theory. Thus, in this work, both the wave amplitude and the floating platform movements are considered small compared to the wavelength and water depth. Additionally, the flow is assumed to be incompressible and irrotational [54,55]. A body's response to waves is a complicated phenomenon involving interactions of the body dynamics with several forces. When the non-linearities of the responses are small, the linear wave theory has proved to be satisfactory to describe the dynamics of OWC systems in fixed and floating devices [54].

The equations of motion are presented in Refs. [42] and [54] for the case of two bodies oscillating in heave. This work considered six bodies: one for the physical floating platform — the floater — and five for the OWCs. Ref. [56] presents the equations of motion for an arbitrary number of oscillating bodies.

The floater can oscillate with six degrees of freedom: surge (mode 1), sway (mode 2), heave (mode 3), roll (mode 4), pitch (mode 5), and yaw (mode 6). As a simplification for the five internal oscillating water columns, only the heave mode was considered (modes 9, 15, 21, 27 and 33). The vector x_i represents all modes for the six-body system with time-dependent components, where i is the mode index from $i = 1, \ldots, 6$ for the floater, and $i = 9, 15, 21, 27, 33$ for the five OWCs. In the absence of waves, $x_i = 0$ for all modes. Note that the OWCs are modeled as fictitious rigid pistons placed on the inner free surface of the pneumatic chamber of each OWC. This approximation has proved to be acceptable [57].

In the case of the six-body problem, the mass-inertia matrix $M_{i,j}$ has 36×36 components [56]. Each entry of the matrix $M_{i,j}$ can be decomposed in mass $m_{i,j}$ plus added mass at infinity frequency $A^{\infty}_{i,j}$ [56]. For the five OWCs, only the components associated with heave modes are considered, i.e., components $M_{9,9}$, $M_{15,15}$, $M_{21,21}$, $M_{27,27}$, and $M_{33,33}$. The coupling added-mass terms $M_{3,9}$ and $M_{9,3}$, $M_{3,15}$, $M_{15,3}$, $M_{3,21}$, $M_{21,3}$, $M_{3,27}$, $M_{27,3}$, $M_{3,33}$, $M_{33,3}$ were assumed to exist only in the heave degrees of freedom [42], i.e., $i = 3, 9, 15, 21, 27, 33$. Note that the inertia matrix $M_{i,j} = m_{i,j} + A^{\infty}_{i,j}$ is symmetric and comprises many zero values. The interaction between the different pistons was neglected in the simulations.

Applying Newton's law, the equation of motion of a floating body is given by equating the inertial forces to the sum of the forces acting on the body. The equations of motion for the ith mode in the time domain can be written as

$$\begin{aligned}
&\sum_{j=1}^{6}\left(\left(m_{3,j}+A^{\infty}_{3,j}\right)\ddot{x}_j+R_{3,j}+C_{3,j}\,x_j\right)\\
&\quad+\left(A^{\infty}_{3,9}\,\ddot{x}_9+R_{3,9}\right)+\left(A^{\infty}_{3,15}\,\ddot{x}_{15}+R_{3,15}\right)\\
&\quad+\left(A^{\infty}_{3,21}\,\ddot{x}_9+R_{3,21}\right)+\left(A^{\infty}_{3,27}\,\ddot{x}_9+R_{3,27}\right)+\left(A^{\infty}_{3,33}\,\ddot{x}_9+R_{3,33}\right)\\
&\quad=F^{\mathrm{exc}}_3+F^{\mathrm{moor}}_3+F^{\mathrm{PTO}}_9+F^{\mathrm{PTO}}_{15}+F^{\mathrm{PTO}}_{21}+F^{\mathrm{PTO}}_{27}+F^{\mathrm{PTO}}_{33}\,,
\end{aligned} \tag{1}$$

$$\sum_{j=1}^{6}\left(\left(m_{i,j}+A^{\infty}_{i,j}\right)\ddot{x}_j+R_{i,j}+C_{i,j}x_j\right)=F^{\mathrm{exc}}_i+F^{\mathrm{moor}}_i,\quad i=1,2,4,5,6, \tag{2}$$

$$\left(m_{k,k}+A^{\infty}_{k,k}\right)\ddot{x}_k+R_{k,k}+C_{k,k}\,x_k+A^{\infty}_{k,3}\,\ddot{x}_3+R_{k,3}=F^{\mathrm{exc}}_k-F^{\mathrm{PTO}}_k, \quad k=9,15,21,27,33, \tag{3}$$

where x_j, $\dot{x}_j$, and $\ddot{x}_j$ are the displacement, velocity, and acceleration of the jth mode, respectively.

The radiation forces $R_{i,j}$ are obtained through the convolution integrals considered as functions of the radiation damping coefficients and are given by

$$R_{i,j}=\int_0^t \kappa_{i,j}(t-\tau)\,\dot{x}_j(\tau)\,\mathrm{d}\tau\,, \tag{4}$$

where

$$\kappa_{i,j}(t)=\frac{2}{\pi}\int_0^{\infty} B_{i,j}(\omega)\cos(\omega t)\,\mathrm{d}\omega\,, \tag{5}$$

represents the radiation impulse response functions (IRFs) and $B_{i,j}$ is the radiation damping coefficient. The components C_{ij} represent the hydrostatic coefficients matrix components as described in Ref. [41].

The terms F^{moor}_i are the force components associated with the mooring lines. The excitation force components F^{exc}_i are exerted by the incident wave on the floater and are determined by the incident wave amplitude A_{w}, and the exciting force or moment Γ_i. These are given in function of the regular wave component with frequency ω_n. As such, the excitation forces F^{exc}_i can be obtained as a sum of N components as a function of the frequency ω_n

$$F^{\mathrm{exc}}_i(t)=\sum_{n=1}^{N} A_{\mathrm{w}}(\omega_n)\,\Gamma_i(\omega_n)\,\cos\left(\omega_n t+\phi_{\mathrm{r}}(\omega_n)\right), \tag{6}$$

where $i = 1, \ldots, 6$. Here $\phi_{\mathrm{r}}(\omega_n)$ is the random phase of the wave generation, a random number between 0 and 2π.

The coupling term F_i^{PTO} is connected to the relative heave motion of the different bodies and can be obtained from

$$F_i^{\mathrm{PTO}} = S_{\mathrm{p},i}\, p_{\mathrm{ac},i}(t)\,, \quad i = 9, 15, 21, 27, 33\,, \tag{7}$$

where $p_{\mathrm{ac},i}(t)$ represents the instantaneous pressure in the ith air chamber relative to the atmosphere. The knowledge of the pressure within the chamber necessary to solve Eq. (7) requires solving simultaneously the complete system of equations, which includes the definition of the air chamber, turbine, generator, and control models [42]. These are discussed and presented in Sections 4.2 and 4.3, based on Ref. [42].

4.2. Air chamber model

The air in the pneumatic chamber is assumed to satisfy the ideal gas equation

$$\rho_{\mathrm{ac}} = \frac{p_{\mathrm{ac}} + p_{\mathrm{at}}}{R\, T_{\mathrm{ac}}}, \tag{8}$$

where ρ_{ac} is the air density, p_{at} the atmospheric pressure (assumed constant), T_{ac} the air absolute temperature, R is the gas constant. In this context, the turbulent and molecular diffusion process is assumed to occur sufficiently rapidly. As a result, the thermodynamic variables within the air chamber can be treated as uniformly distributed across space (air chamber).

The conservation of mass in the air chambers may be expressed as [58]

$$\dot{\rho}_{\mathrm{ac}}\, V + \rho_{\mathrm{ac}}\, \dot{V} = -\dot{m}_{\mathrm{t}}, \tag{9}$$

where V is the time-dependent volume of air in the chamber and $\dot{m}_{\mathrm{t}}$ is the turbine mass flow rate. The partial air renewal in the chamber during each wave cycle maintains the average air temperature close to the external air temperature. Consequently, the heat exchange across the chamber, turbine walls, and the inner air–water-free surface is negligible compared to the work done by the motion of the inner free surface or the work performed by the turbine [42]. Consequently, the thermodynamic process within the inner air chamber can be approximated as adiabatic.

Furthermore, since (i) the density of air is significantly smaller compared to that of water, and (ii) the vertical dimensions of a full-sized OWC air chamber typically do not exceed a few meters, the differences in potential energy within the air chamber can be neglected [58].

Consequently, the first law of thermodynamics allows the time-derivative of the internal energy $U(t)$ of air in the chamber to be written as

$$\dot{U} = \begin{cases} -\,\dot{m}_{\mathrm{out}}\,(h_{\mathrm{out}} + \frac{1}{2}\,v_{\mathrm{out}}^2) - \rho_{\mathrm{ac}}\,\dot{V}, & \text{if } \rho_{\mathrm{ac}} > \rho_{\mathrm{at}} \text{ (exhalation)} \\ \dot{m}_{\mathrm{in}}\,(h_{\mathrm{in}} + \frac{1}{2}\,v_{\mathrm{in}}^2) - \rho_{\mathrm{ac}}\,\dot{V}, & \text{if } \rho_{\mathrm{ac}} \le \rho_{\mathrm{at}} \text{ (inhalation)} \end{cases}, \tag{10}$$

where h_{out}, v_{out}, h_{in} and v_{in} are the specific enthalpies and the air velocity at the air chamber outlet during exhalation and the turbine outlet during inhalation, respectively.

The airflow is non-isentropic due to losses primarily occurring in the air turbine. Therefore, the specific entropy in the air chamber is higher than in the atmosphere [58]. The variation in the specific entropy in the air chamber is given as

$$\Delta s_{\mathrm{ac}} = c_v \ln\left(\frac{T_{\mathrm{ac}}}{T_{\mathrm{at}}}\right) + R \ln\left(\frac{\rho_{\mathrm{at}}}{\rho_{\mathrm{ac}}}\right), \tag{11}$$

where T_{at}, ρ_{at}, and c_v correspond to the atmospheric air temperature, air density, and the specific heat at constant volume, respectively.

4.3. Power take-off system modeling

The power take-off (PTO) system utilizes an air turbine to drive an electric generator. Ensuring effective control of the turbine's rotational speed is critical to this system [42].

4.3.1. Turbine modeling

The performance of an air-turbine is typically presented in terms of its dimensionless pressure head Ψ, dimensionless flow rate Φ, dimensionless power output Π and efficiency η_{t}. These are defined as (incompressible flow is assumed) [42]

$$\Psi = \frac{p_{\mathrm{ac}}}{\rho_{\mathrm{a,in}}\, \Omega^2\, d_{\mathrm{t}}^2}, \tag{12}$$

$$\Phi = \frac{\dot{m}_{\mathrm{t}}}{\rho_{\mathrm{a,in}}\, \Omega\, d_{\mathrm{t}}^3}, \tag{13}$$

$$\Pi = \frac{P_{\mathrm{t}}}{\rho_{\mathrm{a,in}}\, \Omega^3\, d_{\mathrm{t}}^5}, \tag{14}$$

$$\eta_{\mathrm{t}} = \frac{\Pi}{\Phi\,\Psi}. \tag{15}$$

Here Ω is the turbine rotational speed (in radians per unit time), d_{t} is the turbine rotor diameter, and P_{t} is the turbine shaft power output. The reference density $\rho_{\mathrm{a,in}}$ is defined in stagnation conditions at the turbine entrance as

$$\rho_{\mathrm{a,in}} = \begin{cases} \rho_{\mathrm{ac}}, & \text{if } p_{\mathrm{ac}} > 0 \text{ (exhalation)} \\ \rho_{\mathrm{at}}, & \text{if } p_{\mathrm{ac}} \le 0 \text{ (inhalation)} \end{cases}. \tag{16}$$

The turbine aerodynamic power is computed from Eqs. (14) and (15) as

$$P_{\mathrm{t}} = \rho_{\mathrm{a,in}}\, \Omega^3 d_{\mathrm{t}}^5\, \Pi(\Psi). \tag{17}$$

The mass flow rate of air through the turbine and the associated specific enthalpy are turbine outputs. The specific enthalpy at the turbine's outlet $h_{\mathrm{t}}^{\mathrm{out}}$ is defined as

$$h_{\mathrm{t}}^{\mathrm{out}} = \begin{cases} h_{\mathrm{ac}} - \left(\dfrac{p_{\mathrm{ac}}}{\rho_{\mathrm{a,in}}}\right)\eta_{\mathrm{t}}, & \text{if } p_{\mathrm{ac}} > 0 \text{ (exhalation)} \\ h_{\mathrm{at}} + \left(\dfrac{p_{\mathrm{ac}}}{\rho_{\mathrm{a,in}}}\right)\eta_{\mathrm{t}}, & \text{if } p_{\mathrm{ac}} \le 0 \text{ (inhalation)} \end{cases} \tag{18}$$

where h_{at} and h_{ac} are the atmospheric and air chamber-specific enthalpies, respectively.

4.3.2. Electric generator and control modeling

When controlling the turbine, the goal is to maximize its efficiency. This implies operating the turbine at the best efficiency point Ψ_{bep}, meaning it should comply with [59]

$$P_{\mathrm{t}} \approx \underbrace{\rho_{\mathrm{at,in}}\, d_{\mathrm{t}}^5\, \Pi\big(\Psi_{\mathrm{bep}}\big)}_{a_{\mathrm{bep}} = \mathrm{const}}\, \Omega^3, \tag{19}$$

where a_{bep} is a constant dependent on the turbine geometry. Note that the atmospheric air density is used to define a_{bep}. Thus, the generator control law must follow the relation [42,60]

$$P_{\mathrm{ctrl}} = a_{\mathrm{bep}} \Omega^3, \tag{20}$$

and the instantaneous rotational speed is computed from [61]

$$\frac{\mathrm{d}}{\mathrm{d}t}\left(\frac{1}{2} I \Omega^2\right) = P_{\mathrm{t}} - P_{\mathrm{ctrl}}. \tag{21}$$

Here P_{ctrl} represents the generator shaft power. It is important to note that most control strategies to date focus on maximizing turbine efficiency, and a combination of comprehensive control strategies should minimize the levelized cost of energy [62].

4.3.3. Turbine damping

The present work utilizes a symmetrical impulse turbine for bidirectional flows [63,64]. This type of turbine has proven to be effective in converting the energy of large air pressure oscillations that occur in energetic sea states [64].

Self-rectifying air turbines of impulse type are characterized for having a relationship between dimensionless values of pressure head and flow rate fairly well-approximated by the expression [65]

$$\Psi = \mathcal{K}_{\mathrm{t}}\, \Phi^2, \tag{22}$$

Table 4
General properties of the platform.

Mode	Stiffness	Unit
Surge	−71973	N/m
Sway	−71322	N/m
Heave	−60800	N/m
Pitch	−1272133	N m/deg
Roll	−1285875	N m/deg
Yaw	−302208	N m/deg

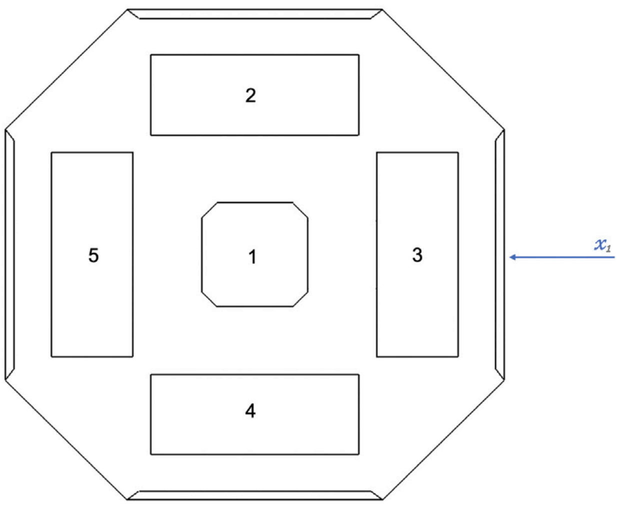

Fig. 8. Orientation and numeration of the OWCs.

where $\mathcal{K}_t$ is a dimensionless constant. From Eqs. (12) and (13) the turbine damping can be obtained as

$$k_t = d_t^2 \left(\frac{\rho_{a,in}}{\mathcal{K}_t \Delta p} \right)^{1/2} . \tag{23}$$

4.4. Linearized mooring model

The mooring forces were considered linear springs such as

$$F_i^{moor} = \kappa_i \sum_{m=1}^{M} x_{m,i} , \tag{24}$$

where $x_{m,i}$ is the displacement coordinate of the mooring line m floater connection point. Four mooring lines were simulated in Modelica and in OpenFAST©, and their main characteristics are the same as those specified for the VolturnUS wind floating platform equally distributed radially (45, 135, 225, and 315 degrees). Hengstmann (2023) [49] presented stiffness coefficients for all DoF for mooring lines with the same characteristics as the VolturnUS platform. As a preliminary approach, the same coefficients were adopted here. The mooring stiffness κ_i in all DoF is shown in Table 4.

5. OctaPlat - Base case definition and analysis

The OWCs were numbered for reference. This is done according to the direction of the incident waves, which is assumed to be coincident with the heading of the x_1-axis. Accordingly, the central OWC is number 1; the top OWC is number 2 when the x_1-axis comes from the right; the following are numbered clockwise from there. This orientation is presented in Fig. 8.

Table 5
Platform natural periods.

	Surge	Sway	Heave	Roll	Pitch	Yaw
T_n [s]	250	250	14.1	20	20	125

5.1. Wind power curve computation

The average power for each wind speed from cut-in to cut-out considering the IEA-15-240-RWT 15 MW reference wind turbine mounted on the OctaPlat and the wind-wave joint climate representation presented in Table 2 was obtained by simulations in OpenFAST©. The power curve is presented in Fig. 9. The plot includes standard deviations for each wind speed. The turbulent wind field for every wind class in Table 2 was generated using normal turbulent conditions, the von Karman turbulent model in the TurbSim pre-processing module. The waves associated with every wind class were considered to follow Pierson-Moskowitz spectra, which was specified in the Hydrodyn module for wind turbine simulation, but also used this spectrum in the evaluation of the wave energy conversion detailed in the next section. The mean annual capacity factor of the wind turbine in the target location is about 0.55, which represent about 8.2 MW of mean annual wind output power.

Free-decay simulations were performed in OpenFAST© for each DoF of the platform. The tests considered a still wind environment with no waves. The natural periods T_n for each of the six DoFs are presented in Table 5.

5.2. Wave energy - Annual production

The OpenModelica platform model was used to calculate the wave annual power generation for different impulse turbine damping for the base case design. The pneumatic power, $\overline{P}_p^{ann}$, corresponds to the energy that is absorbed from the motion of the OWCs. In contrast, $\overline{P}_t^{ann}$ represents the turbine power — it is therefore expected that this parameter will be lower due to the losses in the turbine. These simulation results are presented regarding turbine damping, as defined in Eq. (23), and its effect on the power output of the wave energy conversion systems. Results present the power output of all five OWCs; see Fig. 10.

The maximum annual average produced power occurred around a damping of $3.5{\times}10^{-3}$ ms and corresponds to a pneumatic power of about 3.5 MW and about 2.1 MW of turbine output power. This result appears to be greater than that of other WEC systems. For example, in Ref. [54], for the same site conditions, the platform with five OWC presented a mean annual average pneumatic power of 410 kW for a water surface area of 264 m^2 when equipped with an impulse air turbine. The Mutriku power plant [66] has a design annual average pneumatic power of 175 kW for an area of 223 m^2 for lower energetic wave conditions. These values are 1.3 and 2.6 times lower than those for the platform studied here. Despite these results, rotor speed and cost factors must be considered when selecting the turbine.

5.3. Natural periods

The natural periods for each OWC were determined according to [54]

$$\omega_{n_i} = \sqrt{\frac{\rho g S_{p,i}}{m_i + A_{i,i}(\omega_{n_i})}}, \tag{25}$$

where $S_{p,i}$ corresponds to the waterplane area, m_i corresponds to the body's i mass, and $A_{i,i}$ is the radiation added mass coefficient obtained with WAMIT© for each OWC, i.e., i = 9, 15, 21, 27 or 33. The mass, m_i, is related to the volume defined by the piston, the free surface, and the walls. This study's parameter is zero since the piston is at the free surface. The natural periods are presented in Table 6 for each OWC.

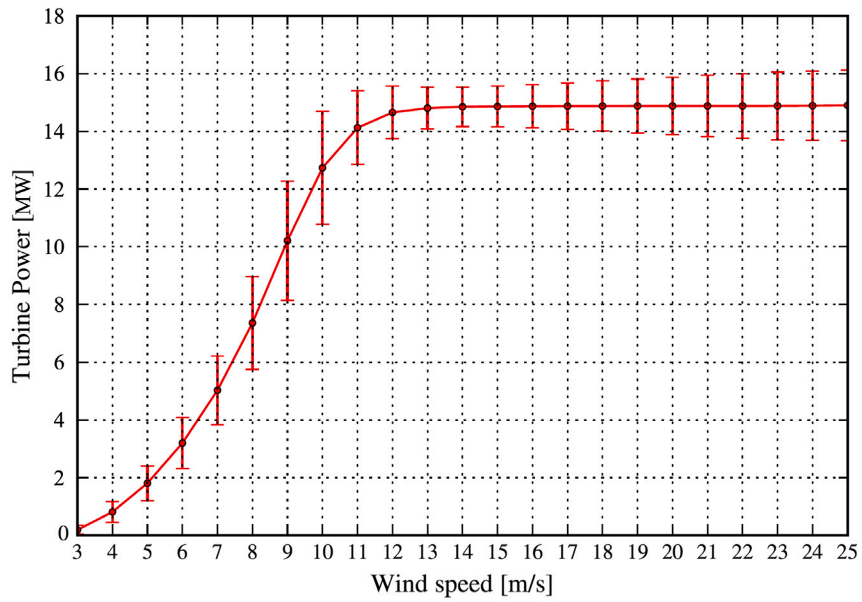

Fig. 9. Power curve of the wind turbine obtained from OpenFAST© results.

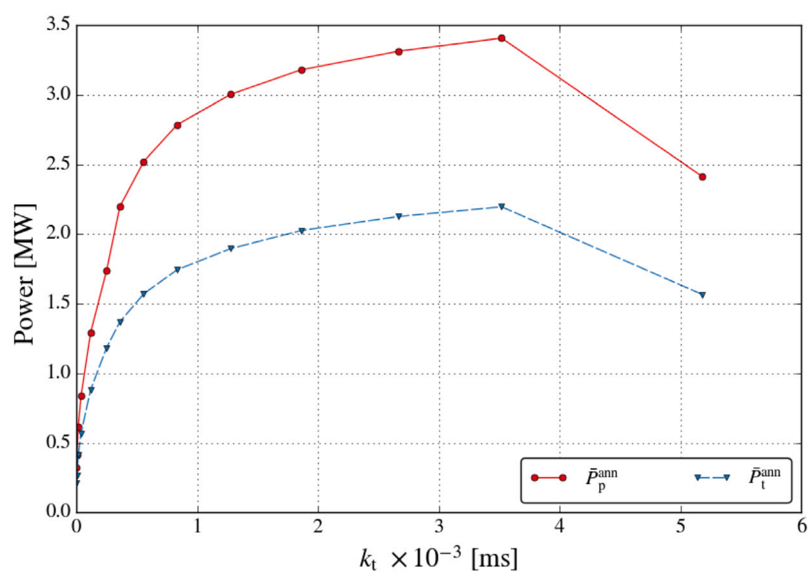

Fig. 10. Average annual pneumatic and turbine power for different turbine damping (Base Case) for the wave energy conversion system.

Table 6
OWCs' natural periods.

	OWC 1	OWC 2	OWC 3	OWC 4	OWC 5
T_n [s]	8.5	8.9	8.9	8.9	8.9

Table 7
Cases studied in simulations with corresponding changed design parameters.

Central OWC		Width lateral OWCs		Water opening height	
Case 1	1.25 a	Case 3	0.75 w	Case 6	0.50 h
Case 2	1.50 a	Case 4	1.25 w	Case 7	0.75 h
		Case 5	1.50 w	Case 8	1.25 h

6. Geometric variables sensitivity analysis

A sensitivity analysis was performed to assess the influence of the selected platform geometric parameters on the overall results, in particular on the wave energy conversion. The reference design — base case — is presented in Fig. 11, which also includes the values of the modified variables. Table 7 shows the cases studied in simulations with the corresponding changed design parameters. All the alterations are presented as a function of the referenced base case.

The results obtained from the OpenModelica platform model for the wave energy production led to the conclusion that the best-performing scenario was the one where the width of the lateral OWCs was set to 1.50 w (Case 5). For the air turbine damping of about 3.5×10^{-3} ms, the total average annual turbine power is approximately 3 MW, which is 50% above the base case. However, the corresponding Aero-Servo-Hydro-Elastic simulations of the floating wind turbine in OpenFAST were unsatisfactory: at higher wind speeds, the platform moved significantly, making its operation undesirable. As such, the best case for this sensitivity analysis was the one with the second-best performance in wave energy generation and for which the platform's movements

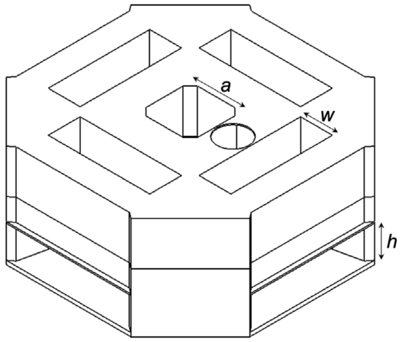

Variable	Reference Value [m]
a	17.8
w	11
h	11

Fig. 11. Selected variables to be altered for the sensitivity analysis and correspondent reference values.

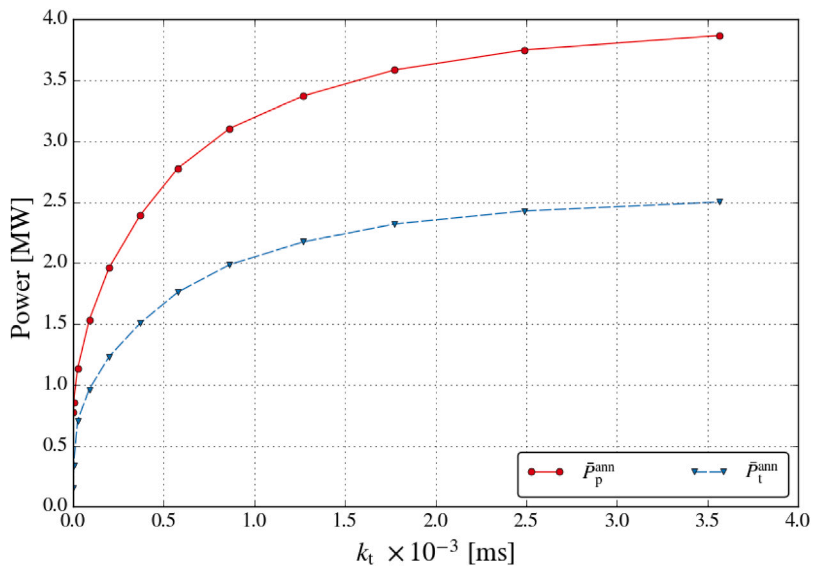

Fig. 12. Case 4: Annual average pneumatic and turbine power for different turbine damping for the wave energy conversion system.

were within operational limits. This corresponded to the case where the width of the lateral OWCs was set to be 1.25 w (Case 4). In this scenario, the platform's air turbines generated an annual average power of approximately 2.5 MW. This turbine power output is observed within an interval of turbine damping between 2.5×10^{-3} and slightly above 3.5×10^{-3} ms. These results are presented in Fig. 12. The hydrodynamic coefficients of Case 4 geometry are presented in Appendix A.

The average wind turbine power obtained for each wind speed was very close to that of the base case (see Fig. 9), and the curves almost overlapped. Similarly, the natural periods obtained were close to those in the base case. In other words, the geometric modifications from the base case to Case 4 did not affect the wind turbine's performance. Therefore, this case was selected for further analysis and the target geometry for the techno-economic analysis.

7. Techno-economic analysis

The LCOE is one of the most important indicators for assessing the feasibility of an energy-related project and is used to compare different technologies [67]. This parameter is the ratio between all the costs incurred during the project's lifetime and the expected energy production. It represents the theoretical cost of electricity produced [68]. The LCOE is calculated as

$$\mathrm{LCOE} = \frac{\sum_{n=0}^{N} \frac{(\mathrm{CAPEX}_n + \mathrm{OPEX}_n + \mathrm{DECEX}_n)}{(1+r)^n}}{\sum_{n=0}^{N} \frac{\mathrm{AEP}_n}{(1+r)^n}}, \tag{26}$$

where CAPEX is the initial investment cost, OPEX corresponds to the expenses with O&M, and DECEX is the decommissioning expenditure. AEP represents the annual net energy produced by the farm, and N is the project's lifetime. The discount rate r includes the inflation rate and the loan rate.

The parameters from Eq. (26) were determined for the geometry selected in the sensitivity analysis presented in the previous section. Details of the most significant cost components' computation and other farm parameters are presented in Appendix C. The LCOE was calculated considering a project lifetime of 30 years [34] and a discount rate of 10% [7,69]. This parameter was firstly determined assuming a turbine damping of 3.5×10^{-3} ms for the wave energy converters (WECs).

The main results can be observed in Table 8. The calculations led to an LCOE of 160 €/MWh for these conditions, which appears is in line with the results obtained for other projects [27]. However, it is still a higher value than other floating offshore wind assessments. According to Ref. [11], in a study from 2022, this value was approximately 125 €/MWh for a wind farm off the west coast of mainland Portugal with one hundred 10 MW turbines mounted on semi-submersible platforms similar to the WindFloat concept [36], using the same discount rate of 10%. However, it is important to recognize not only that the wind turbines in that study may benefit from economies of scale, thereby reducing the LCOE, but also that the cost of offshore wind has recently trended upward in response to supply chain disruptions and adverse macroeconomic conditions.

Nevertheless, considering the positive results obtained in terms of energy production when compared to other works, there seemed to

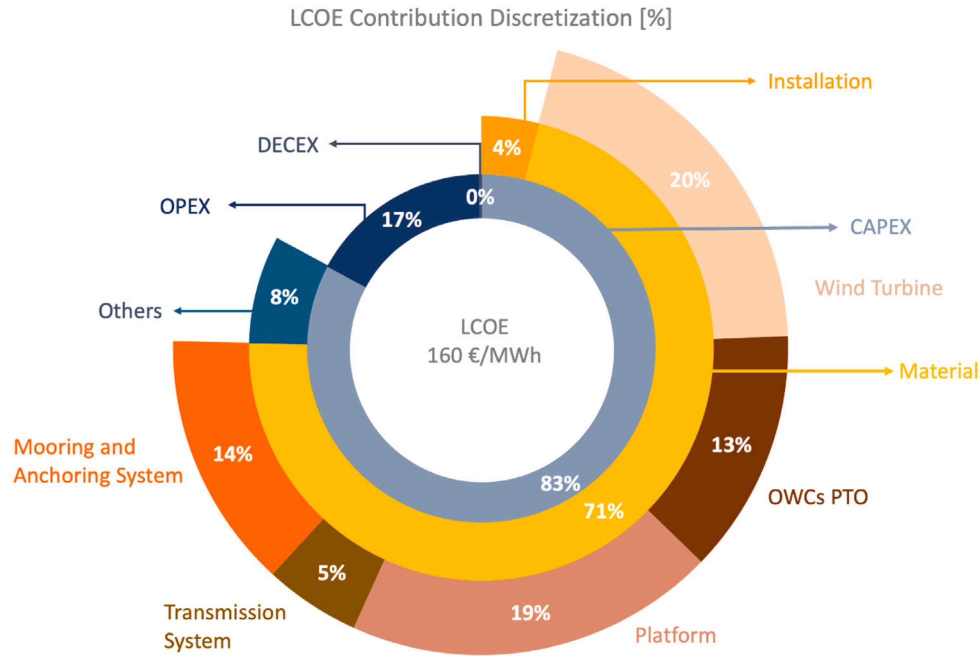

Fig. 13. The LCOE is split into three layers. The inner layer corresponds to the overall CAPEX, OPEX, and DECEX. The second layer discriminates CAPEX into materials and installation. The outer layer includes all the elements that contribute to the materials CAPEX.

Table 8
LCOE, annual energy yield (AEP), total CAPEX, net present value of operation and maintenance costs over the lifetime ($OPEX_{NPVtot}$), and net present value of decommissioning costs ($DECEX_{NPV}$).

$CAPEX_{tot}$ [M€]	1798
$OPEX_{NPVtot}$ [M€]	363.2
$DECEX_{NPV}$ [M€]	8.1
AEP [GWh/year]	1439
LCOE [€/MWh]	160

be room for improvement. As such, the LCOE was divided into its components to obtain a more details of the origin of this value. Fig. 13 shows that discrimination.

As it can be observed in Fig. 13, CAPEX contributed to about 83% of the overall LCOE, with OPEX and DECEX accounting for the remaining 17%. The major contribution of CAPEX was disaggregated into materials, installation and others (engineering management, development, insurance, and contingencies), as represented in the second layer of the figure. Among these, materials costs represented around 86% of the total CAPEX and 71% of the LCOE, with installation CAPEX and Others representing just around 4% and 8% respectively of this value. The materials CAPEX was further detailed regarding the elements forming this category (the graphic's outer layer).

The results showed that nearly 40% of the LCOE was the responsibility of the Wind Turbines (20%) and Platform (19%), with the OWCs accounting for the third largest share of materials CAPEX (comprising 13% of the total LCOE). While the platform and wind turbine were expected to contribute greatly to these costs, the results indicated that the OWCs significantly impacted the overall LCOE. It was further concluded that most of such costs correspond to the turbines utilized for energy conversion. A 25% and 50% reduction in the air turbine costs led to LCOEs that were 8% and 13% lower than the initial ones. In this sense, it seems obvious that reducing wave energy power take-off systems' costs is of utmost importance for the viability of hybrid wind-wave projects.

Considering the farm rated capacity of 450 MW, the unit CAPEX is approximately 4000 €/MW, and unit annual OPEX is about 90 €/kW-year. The LCOE distribution shown in Fig. 13, unit CAPEX, and unit annual OPEX fall within the ranges, or are comparable to the values, reported in recent studies on offshore wind [70,71]. However, the first do not specifically reflect floating wind, due to the current lack of large commercial projects in that segment. The second has made projections for the United States for both fixed-bottom and floating wind farms. It is important to note that the small-sized farm considered in this study, based on a publicly available design configuration with excessively close turbine spacing, may not represent the ideal scenario for evaluating a floating hybrid wind-wave system. Larger farms with lower wake-loss configurations and optimized wave energy conversion systems, for example, are expected to benefit more from the hybrid system's potential to reduce energy costs.

In addition, a Monte Carlo probabilistic analysis was performed to estimate the upper and lower bounds of the LCOE. An $LCOE_{P90}$ represents the 90% chance that the actual value will be higher than this, while an $LCOE_{P10}$ indicates that there is a 10% chance that costs will be this high or higher. Triangular probabilistic distributions were used for CAPEX, OPEX, AEP, and discount rates. The low and high values, with regard to the mid values presented in Table 8, for CAPEX and OPEX were 50% and 150%, and for AEP were 85% and 115%, respectively. Regarding the discount rate, the low, medium and high values were 6%, 10%, and 15%. The results of 5000 runs showed values of 118 and 214 €/MWh for $LCOE_{P90}$ and $LCOE_{P10}$, respectively, being $LCOE_{P50}$ about 160 €/MWh. This confidence interval may be regarded as a way to cope up with various limitations of the current study, which increase the uncertainty. One of these is the fact that for the cases studied, the effect on the directionality of the waves was not considered; nevertheless, the symmetric nature of the OctaPlat and the four peripheric OWCs equally distributed reduces the potential losses due to the directions of the waves. Other factors may be related to the variability in other key inputs like material costs, energy yield estimates, or operational factors (e.g., downtime from environmental factors, such as biofouling).

7.1. Best turbine damping

Since the damping of the OWC turbines strongly impacts the LCOE, a more detailed study of the ideal damping was performed to minimize this parameter. The analysis led to the optimal scenario where the turbine damping could differ for each OWC. This is because not all OWCs are equally affected by the incoming waves, and the optimum damping values would vary considerably. For such a case, an LCOE of 135 €/MWh was obtained, corresponding to a reduction of around 16% compared to the previous results. The farm's AEP determined for this scenario was also higher than the one presented in the previous results (where all turbines were assumed to have the same turbine damping) - 1496 GWh were extracted in this best case (near 4% increase when compared to the previously presented output). A similar Monte Carlo probabilistic assessment was done for this scenario. CAPEX, OPEX, AEP and discount rate were varied similarly (i.e., ±50% for CAPEX and OPEX, ±15% for AEP, and discount rate from 0.6 to 0.15). The results of 5000 runs showed values of 99 and 180 €/MWh for $LCOE_{P90}$ and $LCOE_{P10}$, respectively, being $LCOE_{P50}$ (the most probable value) about 135 €/MWh.

In industrial practice, different turbine damping might not be viable when this relies only on the turbine size. To simplify logistics, a standard turbine size could be selected at the expense of higher production levels. Moreover, this analysis was performed assuming only one wave direction.

8. Conclusions

The present study focused on hybrid wind-wave systems. The main objective of the work was to perform a techno-economic analysis of a floating hybrid wind-wave platform whose design is based on the OctaPlat platform developed at the Instituto Superior Técnico. A case of a farm comprising 20 wind-wave systems located 35 km off the west coast of mainland Portugal near Porto was studied. The process began with defining the base case design, which was then subjected to a sensitivity analysis of critical geometric parameters affecting wave energy conversion. This led to the selection of a "best case". This scenario was the object of the techno-economic analysis carried out in this work.

The base case design of the floating platform consists of an 84 m long octagonal concrete platform with five OWCs — four rectangular shaped on the sides and one in the center of the octagonal shape. Once in place, the platform has a draft of about 20 m with a 15 m upper section above the still water level. The hydrodynamic coefficients computation allowed to decouple wind-wave power generation. In particular, the simulation of the annual average power generation for different turbine damping led to the conclusion that the best performance occurred for higher damping values with an average yearly wave energy turbine power generation above 2 MW for the range of damping simulated. The ratio between the annual average pneumatic power and water surface area for the other two previous studies was 1.3 and 2.6 times lower than for the platform studied in this work, which is a positive indicator of its performance.

The sensitivity analysis performed on the platform's dimensions focused on three parameters: the dimension of the central OWC, the width of the lateral OWCs, and the height of the opening of the OWCs below the mean sea level. The cases underwent a hydrodynamic assessment and were first compared regarding wave energy conversion. The best case consisted of a 25% increase in the lateral OWC's width and generated nearly 2.5 MW of mean annually under similar OWCs' turbine damping conditions. This scenario presented the best results regarding wave energy conversion and platform movements. The wind turbine power curve obtained for this case was close to that obtained for the base case, and the total mean wind-wave power output was about 10.75 MW for the selected site. This represents a hybrid floating platform of 22.5 MW of rated power with an averaged capacity factor of about 0.48.

The comparison between numerical and experimental results for a platform of the same kind and same OWCs' dimensions, but with three OWCs aligned with the incident waves, revealed a high degree of agreement, with both showing a coefficient of determination (R^2) value of approximately 0.94 in the 2.5 and 3.4 m irregular wave tests performed.

The LCOE was determined for the best case from the sensitivity analysis previously performed. The results indicated a significant impact of the OWCs' turbines on the overall LCOE. As such, the optimal combination of turbines' damping for each OWC led to an LCOE of 135 €/MWh. To provide a range for the project's valuation, a Monte Carlo probabilistic analysis of CAPEX, OPEX, AEP and discount rate was done. CAPEX and OPEX were randomly varied by triangular distribution density functions ±50%, AEP ±15%, and discount rate between 0.6 and 0.15. The results of 5000 runs showed values of 99 and 180 €/MWh for $LCOE_{P90}$ and $LCOE_{P10}$, respectively, being $LCOE_{P50}$ (the most probable value) about 135 €/MWh.

This work presented a novel hybrid wind-wave floating platform for renewable energy generation with a potential competitive LCOE. While challenges remain, this work contributes with valuable insights into the potential for integrated renewable energy systems and their crucial role in achieving global climate and sustainability goals.

CRediT authorship contribution statement

M.B.V.A. Rodrigues: Writing – original draft, Visualization, Validation, Software, Methodology, Investigation, Formal analysis, Data curation. **J.C.C. Portillo:** Writing – original draft, Visualization, Validation, Supervision, Software, Resources, Methodology, Investigation, Formal analysis, Data curation, Conceptualization. **J.C.C. Henriques:** Writing – review & editing, Validation, Software, Investigation, Formal analysis, Conceptualization. **L.M.C. Gato:** Writing – review & editing, Validation, Supervision, Resources, Project administration, Methodology, Investigation, Funding acquisition, Formal analysis. **N.P. Mendonça:** Writing – original draft, Validation, Methodology, Investigation.

Declaration of competing interest

The authors declare the following financial interests/personal relationships which may be considered as potential competing interests: Juan C. C. Portillo reports was provided by Instituto Superior Técnico, University of Lisbon. If there are other authors, they declare that they have no known competing financial interests or personal relationships that could have appeared to influence the work reported in this paper.

Acknowledgments

The authors acknowledge "Fundação para a Ciência e a Tecnologia" (FCT) for its financial support via LAETA (project UID/50022/2025). The second author is partially supported by the Resilience Recovery Plan (RRP) for Portugal.

Appendix A. OctaPlat's hydrodynamic coefficients (Case 4)

Figs. 14 and 15 presents the added mass, radiation damping, excitation force and phase angle hydrodynamic coefficients for the OctaPlat. They were computed using WAMIT© v7 for an incoming wave direction of zero degrees (as depicted in Fig. 8), using the low-order method and 14 016 source panels to describe the geometry.

Appendix B. Experimental tests and numerical results comparison

The experimental campaign was intended to prove the concept of Octaplat's wave energy production. The tests did not incorporate a wind turbine. The tests were carried out on a 20 m long wave flume with a width of 0.7 m and a depth of water of 0.5 m at the Hydraulic Laboratory of the Instituto Superior Técnico (IST). Due to the wave flume's geometrical constraints, accommodating all five OWCs in the

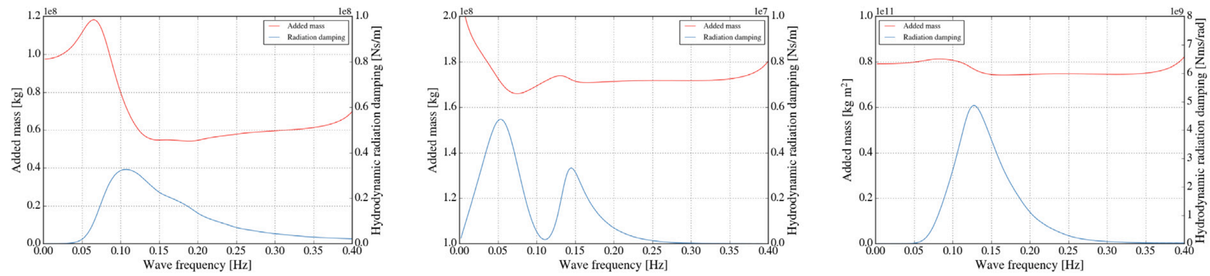

Fig. 14. OctaPlat's added mass and radiation damping hydrodynamic coefficients. Left: Surge, Middle: Heave, and Right: Pitch modes.

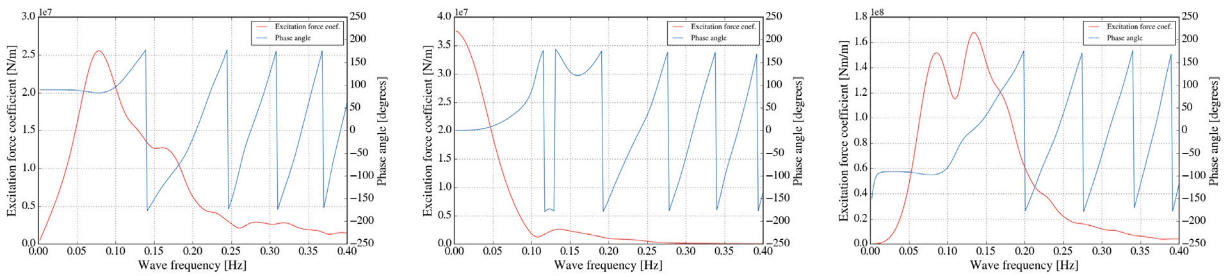

Fig. 15. OctaPlat's excitation force and phase angle hydrodynamic coefficients. Left: Surge, Middle: Heave, and Right: Pitch modes.

Fig. 16. Physical model used during one of the experimental tests [72].

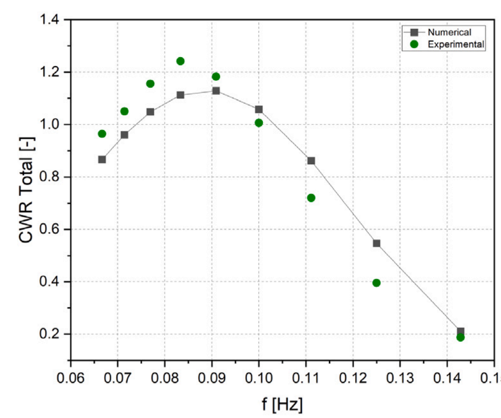

Fig. 18. 3.4 m irregular wave and 30 mm diameter CWR Total comparison.

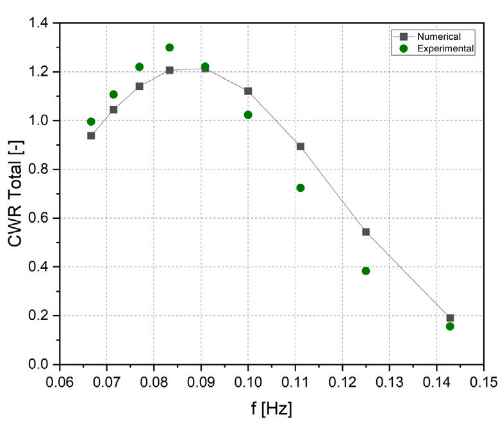

Fig. 17. 2.5 m irregular wave and 30 mm diameter CWR Total comparison.

Table 9
CAPEX material costs of main component formulae.

Component	Expression	Reference	Notes
Wind turbine	$C_T = (1.6\,P_T - 1.9)\,n_T$	[73]	(1)
Oscillating Water Column (OWC)	$C_{OWCs} = \left(\sum_{i=1}^{3} C_{OWC,i}\right) r_P\, n_P$	–	(2)
OWC's air turbine	$C_{turbine} = C_{t,0}\left(\frac{D_t}{D_{t,0}}\right)^2$	[74]	(3)
Floating platform	$C_{Platform} = \left(\sum_{i=1}^{3} C_{P,i}\right) r_P\, n_P$	[73]	(4)
Transmission system	$C_{TS} = \left(\sum_{i=1}^{5} C_{TS,i}\right)$	[73]	(5)
Mooring lines	$C_M = M_M \times l_M \times c_M \times n_M$	[73]	(6)
Mooring anchors	$C_A = m_A \times c_A \times n_A$	[73]	(7)

tested model would have required an excessively small-scale ratio. Consequently, the model was adapted to have three OWCs in the direction of the incoming waves, removing the two lateral OWCs, considering the wave flume as a Ref. [72]. The main dimensions of the OWCs and the separation distances of Case 4 were preserved. The Octaplat platform was tested on a $\lambda = \frac{1}{100}$ Froude scale model (see Fig. 16). The reader should be aware that the use of the Froude number in the scaling of offshore structures and wave energy converters is a common approach, and this leads to a mismatch between Reynolds numbers at small and full scale. Details on this may be found, for example, in Ref. [72].

To account for turbine effects in the scaled model, an orifice was used, following the methodology outlined in Ref. [76,77]. Given that

Table 10
CAPEX installation costs of main components formulae.

Component	Expression	Reference	Notes
Wind turbine	$C_{IT} = \left(\sum_{i=1}^{3} C_{IT,i}\right)$	[73]	(8)
OWC's Air Turbine and upper plate works	$C_{IOWC} = \left(\sum_{i=1}^{3} C_{IOWC,i}\right)$	–	(9)
Floating platform	$C_{IP} = \left(\sum_{i=1}^{3} C_{IP,i}\right)$	[73]	(10)
Transmission system	$C_{ITS} = \left(\sum_{i=1}^{5} C_{ITS,i}\right)$	[73]	(11)
Mooring lines and anchors	$C_{IMA} = \left((C_{IMA,\ 1} + C_{IMA,\ 2})\frac{n_M}{r_{IMA}}\right) + C_{IMA,\ mob}$	[73]	(12)

Notes:
(1) Based on a linear regression model with available dataset as in Ref. [73]. Cost expressed in function of rated power.
(2) Formula based on the expression used to calculate the cost for the floating platform in Ref. [73]. The component i assumes 1 (materials), 2 (direct labor), or 3 (activities costs for the platform). r_p is the industrial profit, dependent on the EURIBOR rate. EURIBOR utilized in this study corresponds to 3.50% as retrieved in December 2023 [75]. Activities costs were assumed 7% of the total material and labor expenses.
(3) $C_{t,0}$ is the cost of a reference turbine taken, $D_{t,0}$ the diameter of the reference turbine, and D_t is the diameter chosen for the OWC design. $C_{t,0}$ = 0.916 M€, $D_{t,0}$ = 1.5 m. Complementary note for the reader: air turbines for OWCs are currently excessively expensive because no commercial stage has been reached. However, in the future, a significant reduction in this cost component is expected as part of learning, technology development, industrialization, and economies of scale.
(4) The component i assumes 1 (materials), 2 (direct labfour), or 3 (activities costs for the platform). Material costs comprise the expenses with the concrete utilized for the structure, and the costs with steel used in the transition piece. The industrial profit, r_p, and activities costs were defined as in Note (2).
(5) i takes values from one to five to account for cabling, onshore and offshore substations, SCADA system, and grid connection costs for the entire transmission system, respectively.
(6) M_M is the mass per unit length [kg/m], l_M is the length of the lines [m], c_M is the cost per kg [€/kg], and n_M is the number of mooring lines. The OctaPlat platform is stabilized with four mooring lines.
(7) m_A is the mass of the anchor [kg], c_A is the cost per kg [€/kg], and n_A is the number of anchors in the system. For each mooring line there is one anchor.
(8) i takes values from one to three to account for the port procedure, transportation, and installation costs, respectively. In Ref. [73], the storage or waiting time of components at port during the installation phases was assumed zero for semisubmersible platforms, and the turbine was assumed to be installed together with the floating platform. In this study the same approach was taken. Thus, transportation and installation costs for the wind turbine ($C_{IT,2}$ and $C_{IT,3}$) are assumed zero.
(9) Formula based on the expression used to calculate the cost of installation for the floating platform in Ref. [73].i takes values from one to three to account for the port procedure, transportation, and installation costs, respectively. The installation times for the OWCs on the platform are considered to be half of that for the wind turbine.
(10) i takes values from one to three to account for the port procedure, transportation, and installation costs, respectively.
(11) i takes values from one to five to account for the array cable, export cable, onshore cables, and offshore and onshore substation installation costs for the whole transmission system, respectively.
(12) $C_{IMA,1}$ is the Anchor Handling Vehicle (AVH) daily cost [€/day], $C_{IMA,2}$ is the direct labor cost [€/day], n_{MA} is the number of anchors and moorings, r_{IMA} is the installation rate [anchors/day], and $C_{IMA,m}$.

the power scale ratio is $\lambda^{3.5}$, and the tested model had a scale 1:100, the corresponding power ratio was 1:10^7. Since the power extracted at this scale is extremely small, using a small-scale turbine would not be practical. Instead, an orifice with a diameter of 30 mm was tested, representing the a full-scale impulse turbine with a rotor diameter of approximately 6.3 m, respectively. The relationship between the diameter of the orifice and the equivalent size of the full-scale turbine was determined based on the methodology presented in Ref. [77].

Numerical simulations were conducted in Modelica, using the same physical model characteristics and hydrodynamic coefficients computed using WAMIT© at full scale. Then, it is possible to compare the capture width ratio (CWR) of the model on the basis of equivalent numerical and experimental results. CWR in this section refers to the mean pneumatic power divided by the mean wave power available to the device [77,78].

Two sets of results are compared in this section regarding the CWR. The cases are those for the orifice of 30 mm and significant wave height of 2.5 and 3.4 m generated using Pierson-Moskowitz spectra under various peak periods. Figs. 17 and 18 present this comparison.

The results of the numerical simulation closely follow the trend lines observed in the experimental work. More importantly, the relative difference between the numerical and experimental results remains within 20% at each frequency, except for an isolated peak deviation, at a frequency of 0.125 Hz. The Coefficient of Determination (R^2) for the experimental and numerical results for the 30 mm turbine simulator is around 0.94 for both 2.5 and 3.4 m irregular waves. This shows the agreement between the two approaches, reinforcing the reliability of the results.

The differences observed between experimental tests and full-scale numerical simulations of OWCs can be attributed to several interrelated factors, particularly involving scaling and modeling limitations. One potential contributor is the mooring system, which affects the energy absorption characteristics of the WEC, and even slight inaccuracies in replicating the small-scale experimental mooring setup in the full-scale numerical model can significantly influence the results [79]. Another critical factor is the treatment of air compressibility within the OWC chambers. In the experiments, chamber volumes were scaled using Froude similarity, which is standard for hydrodynamic modeling, but this approach neglects aero-thermodynamic similarity, which would influence experimental outcomes [77]. However, on a full scale, air compressibility plays a vital role in the dynamic response of the OWC [76], and its exclusion in the experimental setup likely contributed to the discrepancies because of the exact air chamber volume equivalency was not completely replicated in the numerical model due to limitations in the latter. Applying aero-thermodynamic similarity in small-scale models is technically challenging, often requiring the air chamber to be connected to a rigid-walled reservoir, through the use of flexible hoses in the case of floating devices [76], which can introduce unwanted forces and moments and demand additional infrastructure, time, and cost. These practical constraints justified the decision to neglect aero-thermodynamic similarity in the experimental campaign. Furthermore, the hydrodynamic coefficients used in the numerical model, obtained via WAMIT©, did not account for the wave flume walls, implicitly neglecting their effects and further contributing to the mismatch between the simulation and the experimental results.

Table 11
Wind farm and CAPEX input variables.

Component	Value	Unit	Reference (Year)
Wind farm and energy yield data			
Lifetime of farm	30	years	[34]
Discount rate	10	%	[69]
Wind turbine rated power	15	MW	[44]
Floating wave energy platform rated power*	7.5	MW	–
Capacity factor of farm's wind energy production*	0.55	–	–
Capacity factor floating wave energy platform*	0.25	–	–
Capacity factor hybrid wind farm*	0.48	–	–
Availability of wind turbines	95	%	[81]
Availability of OWCs	90	%	–
Wake losses	15	%	[82]
Airfoil damage losses	2	%	[83]
Transmission losses	3	%	[84]
Cables, mooring lines and anchoring systems data			
Array cables length	25,042	m	–
Offshore export cable length	35,000	m	–
Onshore export cable length	2000	m	–
Mooring lines length	850	m	–
Anchors weight	24,000	kg	[85]
Capex materials inputs and data			
Steel cost	2200	€/ton	[86] (2023)
Concrete cost	240	€/ton	[87] (2023)
Array cable cost	279	€/m	[73] (2020)
Offshore export cable cost	336	€/m	[73] (2020)
Onshore export cable cost	83	€/m	[73] (2020)
Offshore substation cost	33.0	M€	–
Onshore substation cost	16.5	M€	–
Direct labor cost	30.5	€/h	[88] (2023)
Capex installation inputs and data			
Installation, transport and port costs of wind turbine	2.6	M€	–
Installation, transport and port costs of OWC air turbine and upper plate works	6.3	M€	–
Installation, transport and port costs of floating platform	9.1	M€	–
Installation costs of mooring lines and anchors	4.9	M€	–
Installation array cable cost	22.0	M€	–
Installation offshore export cable cost	16.8	M€	–
Installation onshore export cable cost	0.5	M€	–
Installation offshore substation cost	3.4	M€	–
Installation onshore substation cost	1.7	M€	
Tug vessel daily cost	22,500	€/day	[73] (2020)
Array cable laying vessel daily cost	91,000	€/day	[73] (2020)
Export cable laying vessel daily cost	114,000	€/day	[73] (2020)
Anchor Handling Vehicle (AVH) daily cost	48,900	€/day	[73] (2020)
Rock dumping vessel daily cost	13,800	€/day	[73] (2020)
Crane at port cost	833	€/h	[73] (2020)
Floating crane with storage area daily cost	811,900	€/day	[73] (2020)
Crew transfer vessel daily cost	36,000	€/day	[89] (2019)
Cable laying vessel mobilization costs	572,000	€	[89] (2019)
Tug vessel mobilization costs	37,000	€	[89] (2019)
Anchor Handling Vehicle mobilization costs	234,000	€	[89] (2019)

* Summary of results from this study.

Appendix C. Costs and farm parameters

Tables 9 and 10 summarize the relations used for the estimation of the CAPEX. Table 11 presents additional parameters considered in the estimation of the LCOE. The costs presented indicate the year when associated with references. Costs without references are product of internal estimations. All costs used in the LCOE computations were updated to 2023 using the Harmonized Index of Consumer Prices (HICP) [80].

Data availability

Data will be made available on request.

References

[1] Intergovernmental Panel on Climate Change. Climate Change 2021: The physical science basis. 2023, https://report.ipcc.ch/ar6wg1/pdf/IPCC_AR6_WG1_Full_Report.pdf.

[2] International Energy Agency. Net Zero by 2050 - Roadmap for the Global Energy Sector. 2023, https://www.iea.org/topics/net-zero-emissions.

[3] European Commission. The European Green Deal. 2019, https://eur-lex.europa.eu/legal-content/EN/TXT/HTML/?uri=CELEX:52019DC0640&from=EN.

[4] International Energy Agency. Renewables 2022: Analysis and forecast to 2027. 2022, https://iea.blob.core.windows.net/assets/ada7af90-e280-46c4-a577-df2e4fb44254/Renewables2022.pdf.

[5] European Commission. An EU strategy to harness the potential of offshore renewable energy for a climate neutral future. 2020, https://eur-lex.europa.eu/legal-content/EN/TXT/HTML/?uri=CELEX:52019DC0640&from=EN.

[6] International Renewable Energy Agency. Fostering a Blue Economy: Offshore renewable energy. 2020, https://www.irena.org/-/media/Files/IRENA/Agency/Publication/2020/Dec/IRENA_Fostering_Blue_Economy_2020.pdf?rev=57eb343cbcbc47bb8d7fa39b4cdd6a03.

[7] International Energy Agency. Offshore Wind Outlook 2019. 2019, https://iea.blob.core.windows.net/assets/495ab264-4ddf-4b68-b9c0-514295ff40a7/Offshore_Wind_Outlook_2019.pdf.

[8] DGEC. Consulta pública sobre a revisão do PNEC 2030. 2023, https://www.dgeg.gov.pt/pt/destaques/consulta-publica-sobre-a-revisao-do-pnec-2030/.

[9] International Renewable Energy Agency. Renewable Power Generation Costs in 2021. 2022, https://www.irena.org/-/media/Files/IRENA/Agency/Publication/2022/Jul/IRENA_Power_Generation_Costs_2021.pdf?rev=34c22a4b244d434da0accde7de7c73d8.

[10] National Renewable Energy Laboratory. 2021 Cost of Wind Energy Review. 2022, https://www.nrel.gov/docs/fy23osti/84774.pdf.

[11] Martinez A, Iglesias G. Mapping of the levelised cost of energy for floating offshore wind in the European Atlantic. Renew Sustain Energy Rev 2022;154:111889. http://dx.doi.org/10.1016/j.rser.2021.111889.

[12] International Renewable Energy Agency. Floating Offshore Wind Outlook. 2024, https://www.irena.org/-/media/Files/IRENA/Agency/Publication/2024/Jul/IRENA_G7_Floating_offshore_wind_outlook_2024.pdf.

[13] European Commission, The E.U. Blue economy report 2025 (2025) https://op.europa.eu/webpub/mare/eu-blue-economy-report-2025/blue-economic-sectors/marine-renewable-energy.

[14] McTiernan KL, Sharman KT. Review of hybrid offshore wind and wave energy systems. J Phys: Conf Ser 2020;1452(1):012016. http://dx.doi.org/10.1088/1742-6596/1452/1/012016.

[15] Perez-Collazo C, Greaves D, Iglesias G. A review of combined wave and offshore wind energy. Renew Sustain Energy Rev 2015;42:141–53. http://dx.doi.org/10.1016/j.rser.2014.09.032.

[16] Hu J, Zhou B, Vogel C, Liu P, Willden R, Sun K, Zang J, Geng J, Jin P, Cui L, Jiang B, Collu M. Optimal design and performance analysis of a hybrid system combing a floating wind platform and wave energy converters. Appl Energy 2020;269:114998. http://dx.doi.org/10.1016/j.apenergy.2020.114998.

[17] Shahir MM, Sarbandi M, Mojallizadeh MR, Hamida MA, Plestan F. Designing a predictive super-twisting sliding mode control for floating offshore wind turbines in region 2. In: Proceedings of the wind energy science conference (WESC) 2025. Nantes, France; 2025, URL https://hal.science/hal-05169436v1 (Accessed: 10 Ocober 2025).

[18] OWC, Wave Energy Scontland. Wave and floating wind energy – Opportunities for sharing infrastructure, services and supply chain. Tech. rep., Wave Energy Scotland; 2023, URL https://www.oceanenergy-europe.eu/wp-content/uploads/2023/06/O-LO-R10-031956-R02-Final-Report.pdf (Accessed: 9 October 2025).

[19] Kheirani S, Houmani A, Jahangir MH. Economical investigation of green hydrogen supply for hydrogen-powered ship by off-grid wave and wind energy hubs. Energy Convers Manag: X 2025;26:101006. http://dx.doi.org/10.1016/j.ecmx.2025.101006.

[20] Dong X, Li Y, Li D, Cao F, Jiang X, Shi H. A state-of-the-art review of the hybrid wind-wave energy converter. 2022, http://dx.doi.org/10.1088/2516-1083/ac821d.

[21] Perez C, Iglesias G. Integration of wave energy converters and offshore windmills. In: 4th International Conference on Ocean Energy, 17 October, Dublin, Ireland. 2012, p. 1–6.

[22] Perez-Collazo C, Greaves D, Iglesias G. Hydrodynamic response of the WEC subsystem of a novel hybrid wind-wave energy converter. Energy Convers Manage 2018;171:307–25. http://dx.doi.org/10.1016/j.enconman.2018.05.090.

[23] Perez-Collazo C, Greaves D, Iglesias G. A novel hybrid wind-wave energy converter for jacket-frame substructures. Energies 2018;11. http://dx.doi.org/10.3390/en11030637.

[24] Zhang H, Zhang N, Cao X. Conceptualization and dynamic response of an integrated system with a semi-submersible floating wind turbine and two types of wave energy converters. Ocean Eng 2023;269:113517. http://dx.doi.org/10.1016/j.oceaneng.2022.113517.

[25] Zhu K, Shi H, Zheng S, Michele S, Cao F. Hydrodynamic analysis of hybrid system with wind turbine and wave energy converter. Appl Energy 2023;350:121745. http://dx.doi.org/10.1016/j.apenergy.2023.121745.

[26] Zhu K, Cao F, Wang T, Tao J, Wei Z, Shi H. A comparative investigation into the dynamic performance of multiple wind-wave hybrid systems utilizing a full-process analytical model. Appl Energy 2024;360:122761. http://dx.doi.org/10.1016/j.apenergy.2024.122761.

[27] Petracca E, Faraggiana E, Ghigo A, Sirigu M, Bracco G, Mattiazzo G. Design and techno-economic analysis of a novel hybrid offshore wind and wave energy system. Energies 2022;15(8). http://dx.doi.org/10.3390/en15082739.

[28] Zhu H, Hu C, Sueyoshi M, Yoshida S. Integration of a semisubmersible floating wind turbine and wave energy converters: An experimental study on motion reduction. J Mar Sci Technol 2019;25. http://dx.doi.org/10.1007/s00773-019-00671-y.

[29] DeepCwind Company. Accelerating the future of floating offshore wind. 2016, URL https://www.deepcwindco.com.

[30] Zhang H, Cao X, Zhou Z, Zhang N. Experimental investigation on hydrodynamic response and motion suppression of a floating wind-wave-tidal hybrid system under freak waves. Renew Energy 2026;256:123944. http://dx.doi.org/10.1016/j.renene.2025.123944.

[31] Nautilus. Offshore wind floating solutions. 2023, https://www.nautilusfs.com.

[32] Faraggiana E, Sirigu M, Ghigo A, Petracca E, Mattiazzo G, Bracco G. Conceptual design and optimisation of a novel hybrid device for capturing offshore wind and wave energy. J Ocean Eng Mar Energy 2024;10. http://dx.doi.org/10.1007/s40722-023-00298-7.

[33] Muliawan MJ, Karimirad M, Gao Z, Moan T. Extreme responses of a combined spar-type floating wind turbine and floating wave energy converter (STC) system with survival modes. Ocean Eng 2013;65:71–82. http://dx.doi.org/10.1016/j.oceaneng.2013.03.002.

[34] Rönkkö J, Khosravi A, Syri S. Techno-economic assessment of a hybrid offshore wind-wave farm: Case study in Norway. Energies 2023;16(11). http://dx.doi.org/10.3390/en16114316.

[35] Principle Power. WindFloat©. 2025, ttps://www.principlepower.com/windfloat.

[36] Windplus: WindFloat Atlantic. WindFloat Atlantic: The wind farm. 2023, https://www.windfloat-atlantic.com/the-wind-farm/#project.

[37] DNV. Comparative study of concrete and steel substructures for FOWT. 2022, https://windworks-jelsa.no/app/uploads/2022/01/Comparative-study-of-concrete-and-steel-substructure-for-FOWT_final-for-distribusjon.pdf.

[38] BW Ideol. BW Ideol congratulates its partners EDF renewables and maple power, winners of the mediterranean tender (AO6). 2024, https://www.bw-ideol.com/en/bw-ideol-congratulates-its-partners-edf-renewables-and-maple-power-winners-mediterranean-tender-ao6.

[39] Sif Group. Monopiles & transition pieces. 2023, https://sif-group.com/en/monopiles-and-transition-pieces/.

[40] Marine Insight. 5 biggest oil platforms in the world. 2022, https://www.marineinsight.com/offshore/5-biggest-oil-platforms-in-the-world/.

[41] WAMIT. WAMIT user manual V7. 2013, https://www.wamit.com/manual.htm.

[42] Portillo JCC, Gato LMC, Henriques JCC, Falcão AFO. Implications of spring-like air compressibility effects in floating coaxial-duct OWCs: Experimental and numerical investigation. Renew Energy 2023;212:478–91. http://dx.doi.org/10.1016/j.renene.2023.04.143.

[43] National Renewable Energy Agency. OpenFAST documentation. 2023, https://openfast.readthedocs.io/en/main/source/user/fast_to_openfast.html.

[44] Gaertner E, Sethuraman L, Anderson B, Barter G, Abbas N, Bortolotti P, Scott G, Feil R, Shields M, Rinker J, Zahle F, Meng F, Skrzypinski W, Bredmose H, Dykes K, Allen C, Viselli A. IEA Wind TCP Task 37: Definition of the IEA 15-Megawatt offshore reference wind turbine. 2020, http://dx.doi.org/10.2172/1603478.

[45] OffshoreWINDbiz. Portugal identifies areas for 10 GW of offshore wind. 2023, https://www.offshorewind.biz/2023/01/30/portugal-identifies-areas-for-10-gw-of-offshore-wind/.

[46] National Oceanic and Atmospheric Administration (NOAA). WAVEWATCH III 30-Year Hindcast Phase 2. 2017, https://polar.ncep.noaa.gov/waves/hindcasts/nopp-phase2.php.

[47] National Oceanic and Atmospheric Administration (NOAA). WAVEWATCH III Hindcast and Reanalysis Archives. 2020, https://polar.ncep.noaa.gov/waves/hindcasts/index.php.shutdown.29Aug2023.

[48] National Oceanic and Atmospheric Administration (NOAA). WW3 Historic Results. 2010, https://polar.ncep.noaa.gov/waves/historic.shtml.

[49] Hengstmann M. Analysis Of Wind-Wave Hybrid Energy Generation Systems. (Master's thesis), Instituto Superior Técnico, University of Lisbon; 2023.

[50] Lucca A, Gaudissart M, Fresnel J. Analysis of a hybrid wind-wave floating platform concept. Instituto Superior Técnico, University of Lisbon; 2023, Tech. rep..

[51] Gomes RPF, Henriques JCC, Gato LMC, Falcão AFO. Hydrodynamic optimization of an axisymmetric floating oscillating water column for wave energy conversion. Renew Energy 2012;44:328–39. http://dx.doi.org/10.1016/j.renene.2012.01.105.

[52] Sebastiani A, Castellani F, Crasto G, Segalini A. Data analysis and simulation of the lillgrund wind farm. Wind Energy 2021;24(6):634–48. http://dx.doi.org/10.1002/we.2594.

[53] Strag JG. Offshore floating wind farms cost reduction assessment. (Master's thesis), Instituto Superior Técnico, University of Lisbon; 2022.

[54] Portillo JCC. Oscillating-water-column systems: single devices, arrays and multi-purpose platforms (Ph.D. thesis), Instituto Superior Técnico, University of Lisbon; 2022.

[55] Reis P. Numerical modelling and optimisation of a Backward Bent Duct Buoy for large scale electricity production. (Master's thesis), Instituto Superior Técnico, University of Lisbon; 2018.

[56] Falnes J. Ocean waves and oscillating systems: Linear interactions including wave-energy extraction. Cambridge University Press; 2002.

[57] Falcão AFO, Henriques JCC. Oscillating-water-column wave energy converters and air turbines: A review. Renew Energy 2016;85:1391–424. http://dx.doi.org/10.1016/j.renene.2015.07.086.

[58] Falcão AFO, Henriques JCC. The spring-like air compressibility effect in oscillating-water-column wave energy converters: Review and analyses. Renew Sustain Energy Rev 2019;112:483–98. http://dx.doi.org/10.1016/j.rser.2019.04.040.

[59] Falcão AFO. Control of an oscillating-water-column wave power plant for maximum energy production. Appl Ocean Res 2002;24(2):73–82. http://dx.doi.org/10.1016/S0141-1187(02)00021-4.

[60] Carrelhas AAD, Gato LMC. Reliable control of turbine-generator set for oscillating-water-column wave energy converters: Numerical modelling and field data comparison. Energy Convers Manage 2023;282:116811. http://dx.doi.org/10.1016/j.enconman.2023.116811.

[61] Carrelhas AAD, Gato LMC, Henriques JCC, Marques GD. Estimation of generator electrical power output and turbine torque in modelling and field testing of OWC wave energy converters. Energy Convers Manag: X 2023;19:100384. http://dx.doi.org/10.1016/j.ecmx.2023.100384.

[62] Rosati M, Henriques JCC, Ringwood JV. Oscillating-water-column wave energy converters: A critical review of numerical modelling and control. Energy Convers Manag: X 2022;16:100322. http://dx.doi.org/10.1016/j.ecmx.2022.100322.

[63] Gato LMC, Ferreira DN, Sá DOC. Biradial turbine rotor aerodynamic design and parametric analysis. Energy Convers Manage 2023;278:116651. http://dx.doi.org/10.1016/j.enconman.2022.116651.

[64] Falcão AFO, Henriques JCC, Gato LMC. Self-rectifying air turbines for wave energy conversion: A comparative analysis. Renew Sustain Energy Rev 2018;91:1231–41. http://dx.doi.org/10.1016/j.rser.2018.04.019.

[65] Carrelhas AAD, Gato LMC, Henriques JCC, Falcão AFO, Varandas J. Test results of a 30-kW self-rectifying biradial air turbine-generator prototype. Renew Sustain Energy Rev 2019;109:187–98. http://dx.doi.org/10.1016/j.rser.2019.04.008.

[66] Torre-Enciso Y, Ortubia I, Aguileta LI, Marqués J. Mutriku wave power plant: From the thinking out to the reality. In: Proceedings of the 8th European Wave and Tidal Energy Conference. 2009, p. 319–29.

[67] Papapetrou M, Kosmadakis G. Chapter 9 - Resource, environmental, and economic aspects of SGHE. In: Tamburini A, Cipollina A, Micale G, editors. Salinity gradient heat engines. Series in energy, Woodhead Publishing; 2022, p. 319–53. http://dx.doi.org/10.1016/B978-0-08-102847-6.00006-1.

[68] Martinez A, Iglesias G. Multi-parameter analysis and mapping of the levelised cost of energy from floating offshore wind in the Mediterranean Sea. Energy Convers Manage 2021;243:114416. http://dx.doi.org/10.1016/j.enconman.2021.114416.

[69] Energy Education, University of Calgary. Discount rate and LCOE of energy projects. 2023, URL https://energyeducation.ca/encyclopedia/Discounting.

[70] International Renewable Energy Agency (IRENA). Renewable Power Generation Costs in 2024. Tech. rep., Abu Dhabi: International Renewable Energy Agency; 2025, URL https://www.irena.org/Publications/2025/Jun/Renewable-Power-Generation-Costs-in-2024.

[71] Fuchs R, Zuckerman G, Duffy P, Shields M, Musial W, Beiter P, Cooperman A, Bredenkamp S. The cost of offshore wind energy in the United States From 2025 to 2050. Tech. Rep. NREL/TP-5000-88988, Golden, CO: National Renewable Energy Laboratory; 2024, http://dx.doi.org/10.2172/2433785, URL https://www.nrel.gov/docs/fy24osti/88988.pdf.

[72] Mendonça NP, Portillo JCC. Experimental investigation of a novel wave energy floating platform for hybrid wind-wave applications: The OctaPlat. In: Proceedings of the 16th European wave and tidal energy conference, 7–11 September 2025, funchal. 2025.

[73] Maienza C, Avossa AM, Ricciardelli F, Coiro D, Troise G, Georgakis CT. A life cycle cost model for floating offshore wind farms. Appl Energy 2020;266:114716. http://dx.doi.org/10.1016/j.apenergy.2020.114716.

[74] Falcão AFO. Modelling of Wave Energy Conversion. Lecture Notes, Instituto Superior Técnico, University of Lisbon. Instituto Superior Técnico, University of Lisbon; 2020.

[75] Euriborrateseu. Euribor. 2023, https://www.euribor-rates.eu/pt/taxas-euribor-por-ano/.

[76] Falcão AFO, Henriques JCC. Model-prototype similarity of oscillating-water-column wave energy converters. Int J Mar Energy 2014;6. http://dx.doi.org/10.1016/j.ijome.2014.05.002.

[77] Portillo JCC, Henriques JCC, Gato LMC, Falcão AFO. Model tests on a floating coaxial-duct OWC wave energy converter with focus on the spring-like air compressibility effect. Energy 2022. http://dx.doi.org/10.1016/j.energy.2022.125549.

[78] Portillo JCC, Collins KM, Gomes RPF, Henriques JCC, Gato LMC, Howey BD, Hann MR, Greaves DM, Falcão AFO. Wave energy converter physical model design and testing: The case of floating oscillating-water-columns. Appl Energy 2020;278:115638. http://dx.doi.org/10.1016/j.apenergy.2020.115638.

[79] Falcão AFO. Wave energy utilization: A review of the technologies. Renew Sustain Energy Rev 2010;14:899–918. http://dx.doi.org/10.1016/j.rser.2009.11.003.

[80] European Central Bank. Inflation and consumer prices. 2024, URL https://www.ecb.europa.eu/stats/macroeconomic_and_sectoral/hicp/html/index.en.html.

[81] Cevasco D, Koukoura S, Kolios AJ. Reliability, availability, maintainability data review for the identification of trends in offshore wind energy applications. Renew Sustain Energy Rev 2021;136:110414. http://dx.doi.org/10.1016/j.rser.2020.110414.

[82] EWEA. Wind energy, the facts. Wind Farm Energy Loss Factors. 2023, URL https://www.wind-energy-the-facts.org/wind-farm-energy-loss-factors.html.

[83] Castorrini A, Cappugi L, Bonfiglioli A, Campobasso MS. Assessing wind turbine energy losses due to blade leading edge erosion cavities with parametric CAD and 3D CFD. J Phys: Conf Ser 2020;1618(5):052015. http://dx.doi.org/10.1088/1742-6596/1618/5/052015.

[84] Papadopoulos A, Rodrigues S, Kontos E, Todorcevic T, Bauer P, Pinto RT. Collection and transmission losses of offshore wind farms for optimization purposes. In: 2015 IEEE energy conversion congress and exposition. ECCE, 2015, p. 6724–32. http://dx.doi.org/10.1109/ECCE.2015.7310601.

[85] International SD. Fact sheet 2: Anchors and moorings. 2023, URL https://www.offshorewindscotland.org.uk/media/nu4ppiyv/02-anchors-moorings.pdf.

[86] Eurometal. European stainless coil prices seen increasing. 2023, URL https://eurometal.net/european-stainless-coil-prices-seen-increasing/.

[87] Sørensen HC, Nielsen K, Friis-Madsen E, Aarup B, Kofoed JP, Jensen CM. Concrete for wave power. Tech. rep, Energy Innovation Cluster; 2019.

[88] Eurostat. Statistics explained, hourly labour costs. 2023, https://ec.europa.eu/eurostat/statistics-explained/index.php?title=Hourly_labour_costs.

[89] Lappalainen J. Economic potential of offshore wind energy in the gulf of bothnia. 2019, URL https://aaltodoc.aalto.fi/items/122aff0a-af31-440a-9a43-c9e9cb238948.